https://doi.org/10.5194/egusphere-2025-6174
Preprint. Discussion started: 17 December 2025

A cyclone phase space dedicated to extratropical cyclones

Myriam Besson [1], Gwendal Rivière [1], and Sébastien Fromang [2]

[1]Laboratoire de Météorologie Dynamique–IPSL, Sorbonne Université/CNRS/École Normale Supérieure–PSL Université/École Polytechnique–Institut Polytechnique de Paris, Paris, France
[2]Laboratoire des Sciences du Climat et de l'Environnement, LSCE/IPSL, CEA–CNRS–UVSQ, Université Paris–Saclay, Gif-sur-Yvette, France

Correspondence: Myriam Besson (myriam.besson@lmd.ipsl.fr)

Abstract. Despite intensive research on midlatitude cyclones since the mid-twentieth century, open questions on their structure and development remain, like the question of their core temperature. It is not clear yet what the proportion of cold-core and warm-core cyclones in midlatitudes is, if occluded cyclones are cold-core or warm-core cyclones and how different the processes leading to cold-core and warm-core cyclones are. To address these questions, a new cyclone phase space denoted as ETC-CPS and adapted to extratropical cyclones is developed by introducing three parameters: the core temperature, the thermal asymmetry and the baroclinic conversion rate. Differences with existing cyclone phase spaces are detailed by analyzing two consecutive storms in the North Atlantic, one ending with a warm seclusion and another with an occlusion. ETC-CPS is then applied to all midlatitude cyclones of the Northern Hemisphere (NH) tracked during winter and summer using ERA5 reanalysis.

The results highlight that most of midlatitude NH cyclones are asymmetric warm-core cyclones. At the time of maximum intensity, the fraction of cyclones with a cold core temperature in the lower troposphere fluctuates around 10–15 % depending on the season while that of warm core cyclones is around 85–90 %. It indicates that, in addition to warm-seclusion cyclones, most occluded cyclones have also a warm core. Both cold-core and warm-core cyclones undergo a well-marked baroclinic growth phase before reaching their maximum intensity but their vertical structure differs during that phase. Warm-core cyclones exhibit a clear vertical westward tilt of the geopotential height anomaly contours as in the classical picture of a developing baroclinic unstable mode. In contrast, cold-core cyclones have a funnel-like vertical structure with the anomalous geopotential height field leaning more westward than eastward which makes them also grow baroclinically but with a non-standard baroclinic structure. Differences between seasons are also noticeable. During winter, cold-core cyclones have much weaker intensity than warm-core cyclones and preferentially develop over continental regions whereas warm-core cyclones develop over the oceanic storm tracks. During summer, both types of cyclones preferentially develop over the oceanic storm tracks and have similar intensities.

1 Introduction

Extratropical cyclones are low atmospheric pressure systems that mainly live outside of the tropics (i.e. beyond 30° N or 30° S) and induce large variations in day-to-day weather in those regions (Ulbrich et al., 2009). The most intense events

https://doi.org/10.5194/egusphere-2025-6174
Preprint. Discussion started: 17 December 2025

generate strong devastating surface winds (Fink et al., 2009) and heavy precipitations (Catto et al., 2012). Since they represent a risk for populations and ecosystems crossing their paths, it is important to study them and to improve their forecasts in order to reduce this risk. Additionally, extratropical cyclones having an impact on climate by transporting heat and moisture poleward (Peixoto and Oort, 1992), it is also important to study their links with larger atmospheric circulations or even with other Earth's components. Finally another major motivation to study extratropical cyclones is related to the potential structural and intensity changes that they may undergo under climate change and that may increase the risks for populations and ecosystems (Priestley and Catto, 2022).

In the Northern Hemisphere, there is a wide variety of extratropical cyclones depending on their localization: North Pacific cyclones, North Atlantic cyclones, Arctic cyclones, Mediterranean cyclones, continental cyclones... Most of extratropical cyclones differ from tropical cyclones which are also atmospheric low pressure systems but smaller in size and driven by different physical processes. Tropical cyclones have an axisymmetric structure and exhibit a well-defined warm core that extends throughout the troposphere (Emanuel, 2003). Some extratropical cyclones do exhibit behaviors similar to tropical cyclones like polar lows, medicanes or Kona lows but their number is limited (Emanuel et al., 2025). The more usual synoptic-scale extratropical cyclones exhibit an asymmetric structure characterized by the presence of warm and cold fronts (Dacre et al., 2012) and do not have a systematic well-defined core temperature. The term 'core temperature' here refers to a temperature difference in the lower troposphere between the core of the cyclone (e.g., close to the sea level pressure minimum) and its surroundings.

The question of the proportion of cold-core and warm-core cyclones in the extratropics is unclear. In the midlatitudes, we usually separate cyclones into two categories depending on how the different stages of their life cycle fit within the two well-known cyclone models, namely the Norwegian cyclone model (Bjerknes and Solberg, 1922) and the Shapiro and Keyser (1990)'s cyclone model (Schultz et al., 1998; Catto, 2016). The Norwegian cyclone model terminates its life cycle with an occlusion, that is when the cold and warm fronts merge to form a single so-called occluded front. The Shapiro and Keyser (1990)'s cyclone model terminates its life cycle with a warm seclusion during which the warm front evolves towards a bent-back warm front that isolates the warm air mass near the cyclone center. The latter model is an example of a warm-core cyclone while the core temperature of the former model is a priori not known and may vary from case to case. Hart (2003) concluded that "cold-core occluded cyclones are the most frequently occurring" and that extratropical cyclones have a cold core during most of their life cycle (see e.g., their Fig. 9). However other studies emphasized that a "warm core is typical of midlatitude cyclones" (Gray et al., 2021). Processes leading to warm-core and cold-core cyclones have been examined in two real midlatitude cyclone cases by Azad and Sorteberg (2009) but, to our knowledge, such a question has not been addressed from a statistical perspective in midlatitudes.

The core temperature question for extratropical cyclones was rather mainly tackled by the Arctic cyclones' research community because cold-core cyclones are common in the Arctic, especially in summer, and can last long (sometimes more than a month) with a barotropic structure, having thus various impacts including on sea ice melting (Aizawa and Tanaka, 2016; Croad et al., 2023b; Rivière et al., 2024). Applying the cyclone phase space (CPS) diagram of Hart (2003) to Arctic cyclones, Wang et al. (2024) found a majority of cold-core cyclones. However, by using a slightly different CPS with only one core temper-

https://doi.org/10.5194/egusphere-2025-6174
Preprint. Discussion started: 17 December 2025

ature parameter located in the middle troposphere, Croad et al. (2023a, b) found that 1/3 of the summer Arctic cyclones are cold-core and upper-level dominated ones and 2/3 are warm-core and lower-level dominated ones. Core temperature statistics in the extratropics are therefore rather unclear and mainly unexplored in midlatitudes.

The focus of the paper is on midlatitude cyclones and investigation of Arctic cyclones is left for a future study. The main questions addressed are the following:

- What is the proportion of cold-core and warm-core cyclones in midlatitudes?
- Are occluded cyclones cold-core or warm-core cyclones?
- What are the main characteristics of cold-core and warm-core cyclones?
- How different are the main processes leading to the formation of cold-core and warm-core cyclones?

To address those questions, we introduce a new CPS that is well adapted to study extratropical cyclones. Hart (2003)'s CPS is particularly adapted to study extratropical transitions, i.e. the process by which a tropical cyclone turns into an extratropical cyclone, as the object goes from a symmetric cyclone with a deep warm core to an asymmetric cyclone with a less well defined core temperature. However, as will be shown in this study, the computation of the core temperature in Hart's CPS is not accurate for strongly asymmetric cyclone and a refined diagnostic is needed for extratropical cyclones studies. Additionally, since baroclinic instability is the most important type of fluid dynamics instability in the genesis and intensification of extratropical cyclones (Charney, 1947; Eady, 1949; Lindzen and Farrell, 1980), it is important to introduce a cyclone parameter related to baroclinic growth. The two baroclinic conversion rates, which respectively transfer potential energy from the mean flow to the cyclone and potential energy of the cyclone to kinetic energy of the cyclone (Simmons and Hoskins, 1978; Cai and Mak, 1990) are both good candidates. Baroclinic conversion rates have already been used as proxies of baroclinic interaction intensity along the cyclones' tracks (Rivière et al., 2015; Schemm and Rivière, 2019) but not presented as a function of other cyclones' parameters. In the present paper, such a parameter will be introduced in the new CPS.

After presenting the reanalysis data and the cyclone tracking algorithm, the new CPS adapted to extratropical cyclones studies inspired from Hart's CPS is introduced in Sect. 2. Sect. 3 is dedicated to the results themselves. The newly adapted CPS is illustrated with two cyclones, one fitting with the Shapiro-Keyser cyclone model and the other with the Norwegian cyclone model. Then statistical results in the CPS are presented by distinguishing wintertime and summertime midlatitude cyclones and warm- and cold-core subsets. These results are summarized and discussed in Sect. 4.

2 Data and methods

2.1 Data

This study uses the ERA5 reanalysis dataset of the European Center for Medium-range Weather Forecast (ECMWF) from 1979 to 2014 (Hersbach et al., 2020). The starting date is chosen in order to avoid less reliable reanalyses before satellites.

https://doi.org/10.5194/egusphere-2025-6174
Preprint. Discussion started: 17 December 2025

The horizontal grid resolution is 0.25°. In addition to surface variables, we used data at the 1,000, 900, 850, 750, 600, 450 and 300 hPa pressure levels. Unless otherwise stated, 3-hourly data are used for the tracking of the cyclones and 6-hourly data for the fields analyses. This difference is justified by the fact that the tracking is more accurate with 3-hourly data but that some fields are only available every 6 hours.

2.2 Methods

2.2.1 Tracking algorithm

In the present study, we used the recently developed TempestExtremes framework (Ullrich and Zarzycki, 2017; Ullrich et al., 2021) that provides an intuitive and versatile command line interface dedicated to atmospheric features tracking. Tracking algorithms typically consist in two steps. The first one aims at detecting candidate points at any given times. The second step links these candidates together to build the actual tracks. It is known as the stitching step. For the particular case of extratropical cyclones, it is well known that the number of detected tracks is sensitive to the tracking algorithm used (e.g., Neu et al., 2013; Pinto et al., 2005), the choice and calibration of which must thus be made with care. In the literature two fields are commonly used to detect candidate points, namely the mean Sea Level Pressure (SLP) or the relative vorticity field at 850 hPa. When using the SLP, the raw field does not need any spatial filtering since it is sensitive to synoptic-scale and planetary-scale circulation systems. In contrast vorticity is more adapted to detect smaller-scales structures and needs a filtering step before being used, as it would otherwise be prone to multiple candidate point detections inside a unique cyclone, especially along fronts.

In this paper, we used SLP for the candidate detection step. Candidate points are defined as locations where the SLP is a local minimum and where there exists a closed contour characterized by a SLP larger by at least 100 Pa than the minimum and located within a 6° great-circle distance[1]. In addition candidates located closer to one another than 4° are merged; only the one with the smallest SLP is kept. For the stitching step, consecutive candidates (i.e. separated by 1 timestep – or 3 hours) are linked together if they are spatially separated by less than 4°. Small or stationary tracks are filtered out if their lifetime is shorter than 24 hours or their length smaller than 8°. Likewise, to remove orographic features, we keep only tracks that spend at least 30 hours (10 timesteps) above a surface pressure higher than 900 hPa. The algorithm was carefully calibrated to represent well-identified individual cyclones tracks by taking the example of the tracks observed during the THINICE field campaign (Rivière et al., 2024).

There is no commonly agreed definition of midlatitude cyclones. Here we restrict our analysis to cyclones whose genesis locations lies in the latitude band 30–60° N. The southern limit is chosen to avoid tropical cyclone detections. The northern limit aims at excluding cyclones that originates in the Arctic. In the remainder of this paper, we call midlatitude cyclones the population of cyclones so obtained.

[1] All the distances measured in degrees are great-circle distance.

https://doi.org/10.5194/egusphere-2025-6174
Preprint. Discussion started: 17 December 2025

2.2.2 An adapted cyclone phase space

Core temperature

The core temperature of a cyclone is hereafter defined as the difference between the temperature at the core of the cyclone and the temperature at its surroundings:

$$DTL = T_C - T_B, \tag{1}$$

where T_C (K) is the temperature at the center of the cyclone and T_B (K) is the mean temperature along a circle centered on the cyclone center at a radius of 5° ($\sim$ 500 km). Sensitivity tests were made with radii up to 10° and did not show any major differences in the results. DTL is hereafter estimated at 750 hPa to make a fair comparison with Hart's parameters. When it is positive (resp. negative), the cyclone has a lower-level warm (resp. cold) core. It is instructive to write DTL in terms of geopotential height Z using hydrostatic balance:

$$DTL = \frac{g}{R}\frac{\partial(Z_B - Z_C)}{\partial \ln p}, \tag{2}$$

where g and R are respectively the gravitational acceleration (m s^{-2}) and the specific gas constant of the air (J K^{-1} kg^{-1}). The vertical derivative can be estimated using finite differences of the geopotential height between 600 hPa and 900 hPa. Analogously to the temperature, Z_C and Z_B stand respectively for the geopotential heights (m) at the cyclone center and averaged along a 5°-circle centered on the cyclone center.

Hart (2003) defined the parameter $-VTL$ as follows to estimate the core temperature:

$$-VTL = \frac{\partial(Z_{MAX} - Z_{MIN})}{\partial \ln p}\bigg|_{900\text{ hPa}}^{600\text{ hPa}}, \tag{3}$$

where the minimum and maximum of Z (denoted as Z_{MIN} and Z_{MAX} respectively) are taken within a radius of 500 km. The vertical bar in Eq. (3) denotes a linear regression between 600 hPa and 900 hPa. As we will see in next section, the two parameters $-VTL$ and DTL can be largely different for extratropical cyclones.

Croad et al. (2023a), inspired by Hart's work, built for their CPS another parameter called R_{O_T}, the thermal Rossby number, that is dimensionless and computed using the vertical derivative of the relative vorticity. They show that their parameter is closely proportional to $T_C - T_B$, so to DTL, but the diagnostic is made in the middle of the troposphere while the DTL diagnostic is applied at low levels (typically 750 hPa).

Thermal asymmetry

The thermal asymmetry of a cyclone is hereafter defined as:

$$B_K = \left\langle T_{750\text{ hPa}} \right\rangle_R - \left\langle T_{750\text{ hPa}} \right\rangle_L, \tag{4}$$

where the subscript L indicates the sector left of the current motion and the subscript R the sector right of the current motion and $\langle\ \rangle_R$ and $\langle\ \rangle_L$ denote areal averages over a semi-circle of radius 5° ($\sim$ 500 km) respectively to the right and left sides of the cyclone motion. B_K vanishes for a perfectly symmetric thermal structure. In contrast, cyclone frontal structures with

https://doi.org/10.5194/egusphere-2025-6174
Preprint. Discussion started: 17 December 2025

a warm (resp. cold) sector to the right (resp. left) of the direction of motion result in positive (resp. negative) values. B_K can also be negative, especially at the end of the life cycle of extratropical cyclones during the rolling up of the fronts around the cyclone center. Using both hydrostatic balance and finite differences, B_K can also be written as:

$$B_K \simeq -\frac{g}{R\Delta \ln p}\left(\left\langle Z_{600\text{ hPa}} - Z_{900\text{ hPa}}\right\rangle_R - \left\langle Z_{600\text{ hPa}} - Z_{900\text{ hPa}}\right\rangle_L\right), \tag{5}$$

where $\Delta \ln p = \ln p_{600\text{ hPa}} - \ln p_{900\text{ hPa}}$.

Hart (2003) defined the thermal asymmetry as:

$$B = \left\langle Z_{600\text{ hPa}} - Z_{900\text{ hPa}}\right\rangle_R - \left\langle Z_{600\text{ hPa}} - Z_{900\text{ hPa}}\right\rangle_L \tag{6}$$

The two parameters B_K and B are proportional to each other but we prefer to use B_K to express the thermal asymmetry in Kelvin, as is DTL.

Baroclinic conversion rate and related parameters

As mentioned in the introduction, the baroclinic instability is a key driver of extratropical cyclones genesis and growth. Quantifying its importance during the life cycle of cyclones is commonly done using the so-called Baroclinic Conversion rate (hereafter referred to as BC, in $\text{m}^2\ \text{s}^{-3}$) which measures the conversion from the mean flow available potential energy to the eddy potential energy (Peixoto and Oort, 1992; Rivière and Joly, 2006b). To compute BC for any given cyclone, one needs to separate the flow between a background flow and a perturbation. Usually this is made using time filtering (Rivière and Joly, 2006a; Schemm and Rivière, 2019), the background flow corresponding to the low-frequency part and the perturbation to the high-frequency part. To keep the CPS parameters as simple as possible and to stay as close as possible to the tracking algorithms output, our strategy is to define the background flow with a spatial average made around the cyclone. More precisely the background flow is defined as follows:

$$\begin{cases} \overline{u} = \langle u \rangle \\ \overline{v} = \langle v \rangle \\ \overline{T}(\mathbf{x}) = \langle T \rangle + \langle \nabla T \rangle \cdot (\mathbf{x} - \mathbf{x}_C), \end{cases} \tag{7}$$

where $\langle\ \rangle$ denotes a surface average over a circle of radius 10° ($\sim$ 1,000 km) whose center is the cyclone center. $\mathbf{u} = (u, v)$ is the horizontal wind vector ($\text{m}\,\text{s}^{-1}$), $\mathbf{x}$ is the position vector (m) and $\mathbf{x_C}$ is the position vector of the cyclone center (m). The background flow definition is set to satisfy the thermal wind balance. Indeed, because the geostrophic wind $\mathbf{u}_g$ satisfies the thermal wind balance:

$$\frac{\partial \mathbf{u}_g}{\partial \ln p} = -\frac{R}{f}\mathbf{k} \wedge \nabla T, \tag{8}$$

where f is the Coriolis parameter (s^{-1}), and because the averaged wind over the circle is close to the averaged geostrophic wind $\left(\langle \mathbf{u}_g \rangle \simeq \langle \mathbf{u} \rangle\right)$, one can write:

$$\frac{\partial \overline{\mathbf{u}}}{\partial \ln p} \simeq \frac{\partial \langle \mathbf{u}_g \rangle}{\partial \ln p} \simeq -\left\langle \frac{R}{f}\mathbf{k} \wedge \nabla T \right\rangle \simeq -\frac{R}{f_C}\mathbf{k} \wedge \langle \nabla T \rangle \simeq -\frac{R}{f_C}\mathbf{k} \wedge \nabla \overline{T}, \tag{9}$$

https://doi.org/10.5194/egusphere-2025-6174
Preprint. Discussion started: 17 December 2025

f_C being the value of f at the cyclone center. In other words, the background flow has a constant horizontal temperature gradient balanced by a constant vertical wind shear. Using that definition for the background flow, the perturbation of a variable X will be denoted with primes such that $X = \overline{X} + X'$ for $X = \{u, v, T\}$. More details on the computation of the background flow in the stereographic projection of TempestExtremes is given in Appendix A.

Using these definitions for the perturbations, we recover the usual form of BC in the eddy potential energy equation (see Appendix B):

$$BC = -\frac{\theta'}{S}\left(\mathbf{u}' \cdot \nabla\overline{\theta}\right), \tag{10}$$

where θ is the potential temperature (K) and $S = -\frac{1}{h}\frac{\partial\langle\theta\rangle}{\partial p}$ (K^2 s^2 m^{-2}) the static stability in pressure coordinates, with $h = \frac{R}{p}\left(\frac{p}{p_0}\right)^{\kappa}$ (m^3 kg^{-1} K^{-1}). It is a source term in the equation governing the Eddy Total Energy (ETE, m^2 s^{-2}) defined in Rivière and Joly (2006b) and Schemm and Rivière (2019) as:

$$ETE = \frac{1}{2}\left(u'^2 + v'^2\right) + \frac{1}{2}\frac{\theta'^2}{S}. \tag{11}$$

It is thus relevant to normalize BC by ETE to obtain the baroclinic growth rate $\sigma = BC/ETE$, which reduces also to the product between the environmental baroclinicity (proportional to the Eady Growth Rate) and the efficiency of the cyclone to extract the available potential energy from its environment (Rivière and Joly, 2006b). We will use σ in addition to BC and ETE when studying the energy life cycle of midlatitudes cyclones in the following.

All baroclinic parameters are defined in a 10°-radius around the cyclone center ($\sim$ 1,000 km) and, unless otherwise stated, they are averaged between 900 and 300 hPa.

The core temperature diagnostic DTL, the thermal asymmetry B_K and the baroclinic conversion rate BC form the new CPS adapted to the study of extratropical cyclones and is hereafter denoted as ETC-CPS.

3 Results

3.1 Case studies

The behavior of two midlatitudes North Atlantic cyclones in Hart's CPS and ETC-CPS is hereafter analyzed. They are worth investigating because they evolved in the same geographical area but had very different frontal structures. One followed the Shapiro–Keyser model evolution (Ciarán, 30 Oct–8 Nov 2023) while the other resembled more the Norwegian model (Domingos, 1–7 Nov 2023) as shown below.

3.1.1 Ciarán, a warm-seclusion cyclone

Storm Ciarán was initiated as a diabatic Rossby wave in the western North Atlantic over the Gulf Stream (Volonté and Riboldi, 2024) and then moved eastward along the Atlantic stormtrack. It hit Western Europe during fall 2023 while reaching a deep low SLP of 954 hPa (Fig. 1a). At the time it reached its minimum SLP (Fig. 1b), the warm air mass of the center was isolated

https://doi.org/10.5194/egusphere-2025-6174
Preprint. Discussion started: 17 December 2025

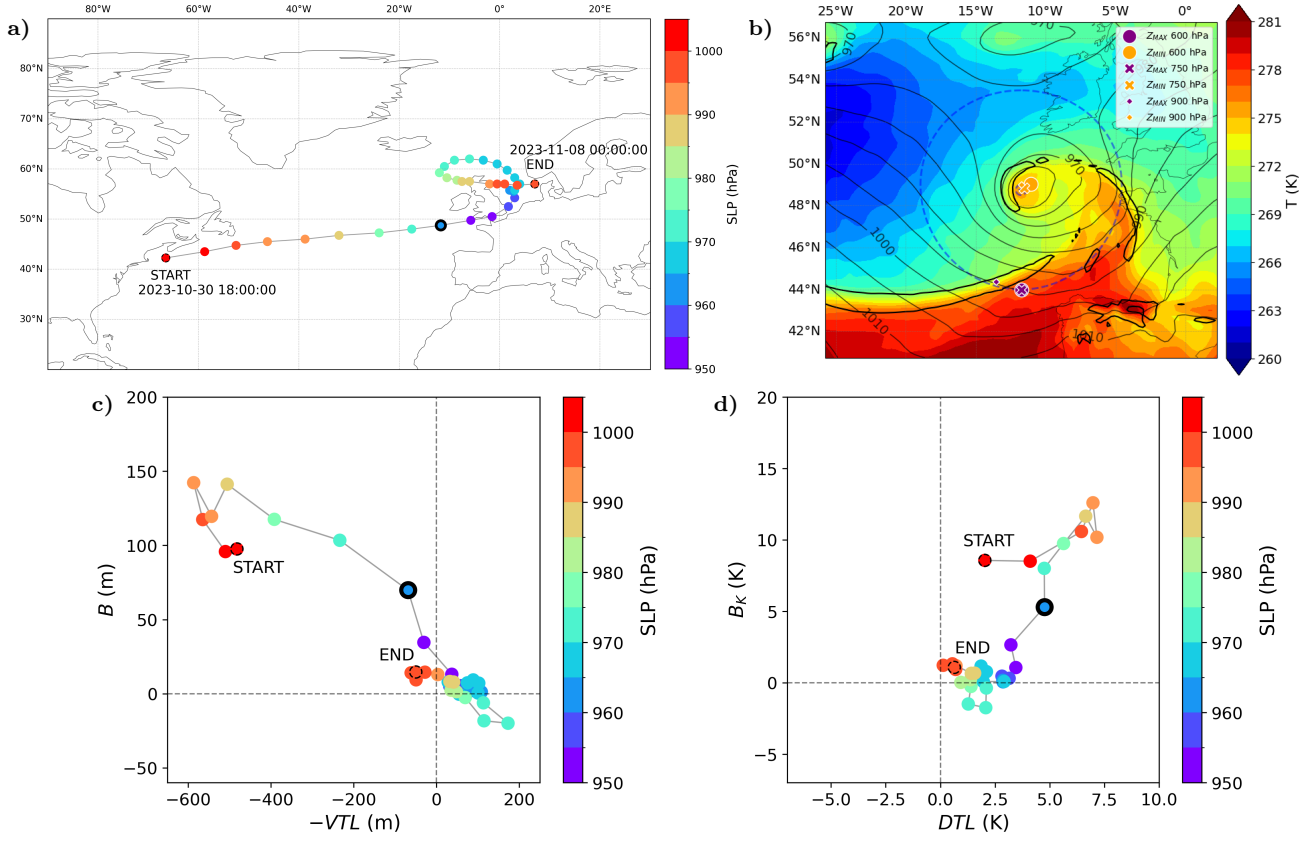

Figure 1. Study of extratropical cyclone Ciarán (30 Oct–8 Nov 2023). **(a)** Ciarán's track. Cyclone centers are tracked every 6 hours. The associated color represents the SLP of the center. Dashed edges highlight starting and ending points. The bold contour highlights the time of the snapshot presented in panel (b). The same shading and edges are used in panels (c) and (d). **(b)** Snapshot of temperature field at 18:00 UTC on 1 November 2023. Shading represents the temperature at 750 hPa. Grey contours show the SLP and the black contour represents the temperature gradient value of 0.05 K km^{-1}. The dashed blue circle is the 5°-radius circle on which T_B is computed. Orange (purple) marks indicate positions of Z_{MIN} (Z_{MAX}) at different pressure levels. **(c)** Ciarán's trajectory in Hart's CPS diagram B vs. $-VTL$. **(d)** Ciarán's trajectory in ETC-CPS diagram B_K vs. DTL.

from the warm sector while the cold front is visible south of the cyclone but detached from the warm front (see the temperature gradient in black contours). The presence of the frontal fracture zone and the warm-air seclusion is typical of a Shapiro–Keyser cyclone type. These characteristics are consistent with the recent results of Volonté and Riboldi (2024) and Gray and Volonté (2024).

Two CPS diagrams are presented for Ciarán: Hart's CPS based on B and $-VTL$ (Fig. 1c) and the ETC-CPS based on B_K and DTL (Fig. 1d). Both B and B_K start from finite, positive values at the beginning of the storm life cycle, and progressively evolve towards lower values until they almost vanish. Such an evolution indicates that Ciarán starts being asymmetric and

https://doi.org/10.5194/egusphere-2025-6174
Preprint. Discussion started: 17 December 2025

gradually evolves towards a symmetric structure. The relatively high values of B_K (10 K) and B (100 m) at the beginning of its life cycle can be explained by the fact that Ciarán formed over the Gulf Stream in a region of high baroclinicity. Later in the life cycle, the decrease in B_K and B are due to colder air moving southward relatively to the cyclone center and warmer air simultaneously approaching that center.

DTL is positive during Ciarán's entire life cycle, decreasing from an initial value of about 5 K to nearly 0 K (Fig. 1d). Ciarán can thus be classified as a warm-core cyclone, a result confirmed by a visual inspection of the temperature at 18:00 UTC on 1 November 2023 (Fig. 1b), which clearly shows that the core is warmer than its environment. Interestingly, $-VTL$ parameter (Fig. 1c) exhibits a different evolution, transitioning from a negative value (-500 m), suggestive of a cold core, to a nearly vanishing value, suggestive of a near-neutral core. This is in striking contrast with the evolution of DTL during the storm life cycle and in disagreement with its structure shown in Fig. 1b.

3.1.2 Domingos, an occluded Norwegian cyclone

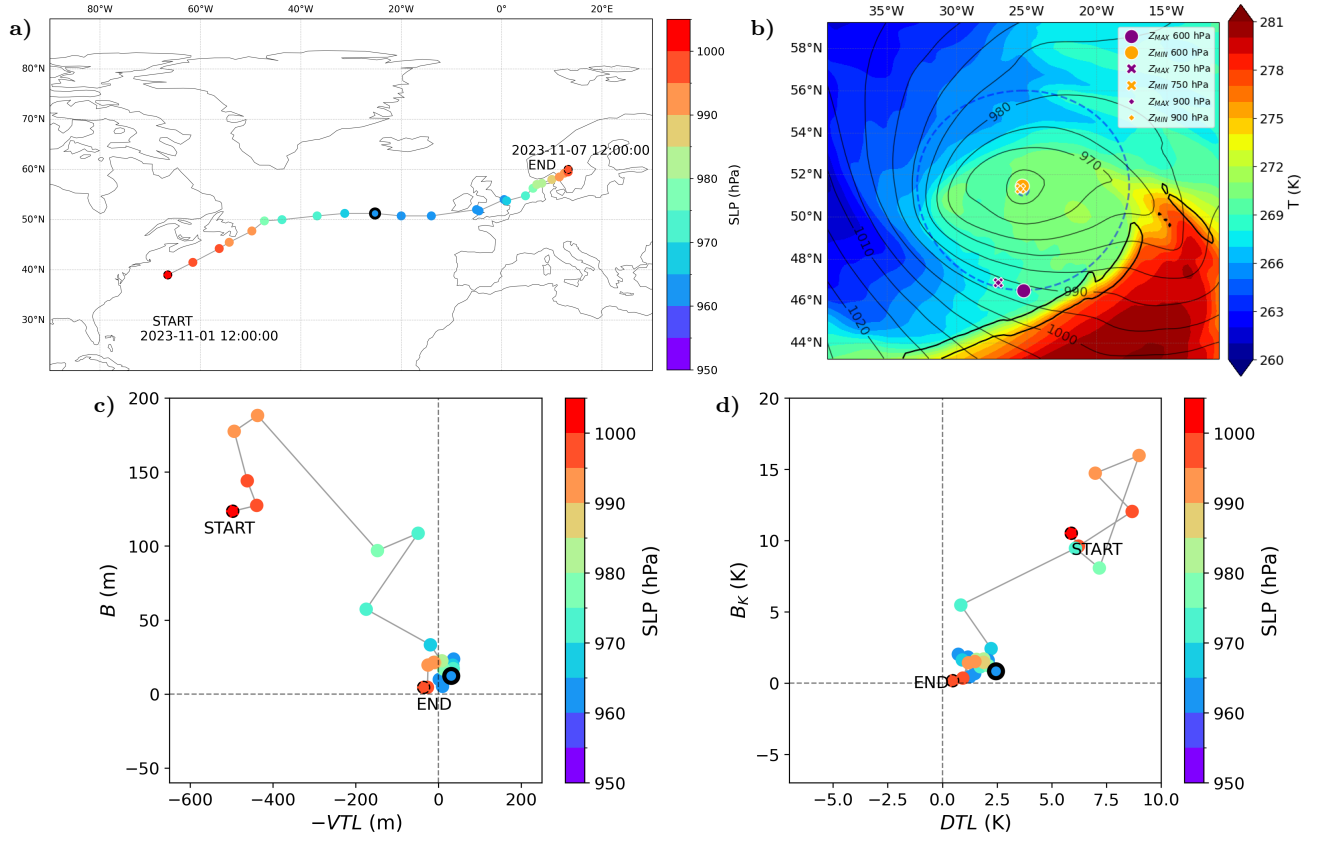

Figure 2. Same as Fig. 1 but for Domingos extratropical cyclone (1–7 Nov 2023). The snapshot of temperature field on panel (b) is made at 18:00 UTC on 3 November 2023.

https://doi.org/10.5194/egusphere-2025-6174
Preprint. Discussion started: 17 December 2025

Storm Domingos formed a few days after Ciarán in the same area. However, in contrast with Ciarán, it developed through a baroclinic interaction with a pre-existing upper-level trough (not shown). Domingos then followed a track similar to Ciarán, moving eastward from the western North Atlantic and hitting Europe with a deepening up to 960 hPa (Fig. 2a). The ends of Ciarán and Domingos life cycles were very different in terms of frontal structures. At the time it reached its minimum SLP, Domingos core structure did not show a coherent isolated warm air mass (Fig. 2b), in contrast with Ciarán (Fig. 1b). The cold front is well visible south of the cyclone and connected to the warm front (see the temperature gradient in black contours). This connection and the fact that the temperature gradient is weak around the cyclone center fits the last stage of the Norwegian cyclone type.

Despite these structural differences, the trajectories of Domingos in both CPS diagrams are very similar to that of Ciarán (compare Fig. 1c with Fig. 2c and Fig. 1d with Fig. 2d). Both B and B_K start large and positive before decreasing to nearly vanishing values, while $-VTL$ (resp. DTL) is initially negative (resp. positive) before evolving towards small values. Near the time at which the central SLP reaches its minimum value, the value of DTL is smaller for Domingos (around 0 K–2.5 K) than for Ciarán (around 2.5–5 K). This is consistent with the presence of a coherent secluded air mass in Ciarán (Fig. 1b) and a more diluted warm air mass around the cyclone center in Domingos (Fig. 2b). To conclude, both cyclones have a warm core temperature during their whole life cycle.

3.1.3 Interpretation

Why are ETC-CPS and Hart's CPS diagrams so different for both Ciarán and Domingos? As shown above, the evolutions of B and B_K are similar for the two storms but DTL and $-VTL$ are dramatically different, particularly during the early stage of their life cycle, to the point that they have opposite signs. There are a priori two main reasons that could explain why DTL and $-VTL$ significantly differ: (i) the positions where $Z = Z_{MIN}$ and $Z = Z_{MAX}$ are not the same at every vertical level and the vertical derivatives of Z_{MAX} and Z_{MIN} cannot be associated with a temperature, (ii) if the positions where $Z = Z_{MIN}$ and $Z = Z_{MAX}$ at the different levels are co-located, Z_{MAX} is not necessarily equal to Z_B and/or Z_{MIN} is not necessarily equal to Z_C.

To better understand the cause of the large difference between DTL and $-VTL$ for Ciarán and Domingos, we looked at the positions of Z_{MAX} and Z_{MIN} at different levels between 600 hPa and 900 hPa. For both storms and for most of the time during their life cycle, Z_{MIN} is systematically located very close to the SLP minimum and Z_{MAX} is generally found south of the cyclone center (see the positions where $Z = Z_{MIN}$ and $Z = Z_{MAX}$ in orange and purple symbols respectively in Fig. 1b and Fig. 2b). Therefore reason (i) cannot explain the discrepancies between DTL and $-VTL$ for Ciarán and Domingos. Since Z_{MIN} is found very close to the cyclone center, we have $Z_{MIN} \simeq Z_C$ but Z_{MAX} is very different from Z_B. Z_{MAX} is situated in a relatively warm region of the 5°-circle, south of the storm center. This preferred location is due to the fact that geopotential values (as well as temperatures) tend to increase equatorward in the midlatitudes. For Ciarán, the location where $Z = Z_{MAX}$ even falls in the warm front of the cyclones, exacerbating the warm temperature at this location.

There is no guarantee that the picture revealed by the two storms is not an exception. We therefore performed a systematic comparison between DTL and $-VTL$ by tracking all midlatitude cyclones (not shown). We found that the case of Ciarán

https://doi.org/10.5194/egusphere-2025-6174
Preprint. Discussion started: 17 December 2025

and Domingos is not peculiar. More precisely we obtained the following results: (i) B_K and B are correlated, (ii) differences between DTL and $-VTL$ can be very large and opposite in sign, especially during the initiation stage of the cyclones, where DTL is generally positive and $-VTL$ generally negative, and (iii) the higher B_K (or B), the higher the difference between DTL and $-VTL$. A large B (or B_K) corresponds to a strong thermal and geopotential asymmetry so that the point of maximum geopotential Z_{MAX} is not representative of the cyclone environment and differences between $-VTL$ and DTL are large in that situation.

We conclude that $-VTL$ is not an appropriate measure of the core temperature with respect to that of the environment, as opposed to DTL. This is because $-VTL$ is more representative of the difference between the core temperature and the warmest temperature in the vicinity of the cyclone, which is likely to be negative.

3.2 General statistics on midlatitude cyclones

The tracking algorithm applied to all seasons from 1979 to 2014 leads to the detection of 35,329 midlatitude cyclones. 25.6 % of them (i.e 9,057 cyclones) have their genesis in winter (December-January-February, DJF) and 22.5 % (i.e. 7,962 cyclones) have their genesis in summer (June-July-August, JJA). Most of the upcoming results are separated between the two seasons DJF and JJA.

3.2.1 Track density maps

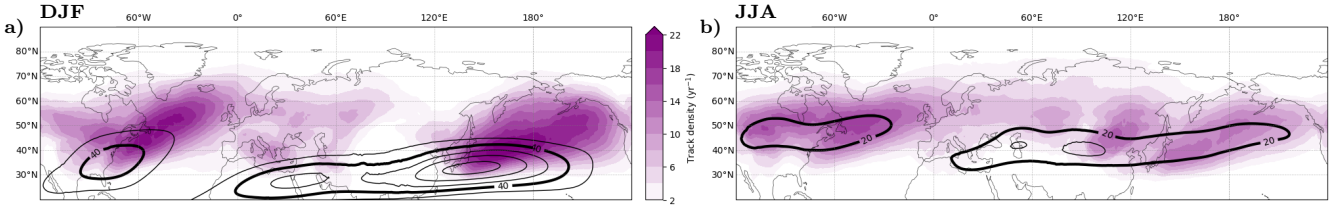

Figure 3. Track density of midlatitude cyclones (shading) in **(a)** DJF and **(b)** JJA. The unit of the shading is the number of tracks per unit area per year, unit area being defined as a 5°-spherical cap ($\sim 10^6$ km^2). A track is counted only once if it goes inside the cap, whatever the number of timesteps spent inside. The counts are divided by the number of years to have an annual rate. In contours is represented the climatological seasonal zonal wind at 200 hPa (every 10 m s^{-1} for positive values only).

In DJF (Fig. 3a) cyclones are mainly found over the oceans in the North Atlantic and North Pacific. These locations correspond to the well-known Northern Hemisphere "storm tracks" (Chang et al., 2002). The entrances of the two storm tracks are associated with strong upper-level westerlies as shown by the high values of zonal wind climatology at 200 hPa. It reflects high values of baroclinicity and the usual key role of baroclinic interaction in those regions. Secondary spots of cyclone activity are also visible and well known in the Mediterranean Sea (Flaounas et al., 2022) and downstream of mountain ranges (Rockies, Ural, Himalayas; see Schär, 2003).

https://doi.org/10.5194/egusphere-2025-6174
Preprint. Discussion started: 17 December 2025

In JJA (Fig. 3b) cyclones are again mainly located over the North Atlantic and the North Pacific, highlighted as well by the high upper-tropospheric zonal wind values, but they are slightly less frequent and the track densities are more zonally oriented than in DJF. The continental cyclone activity becomes of equivalent importance as the oceanic one. The Mediterranean Sea spot disappears.

There are thus important seasonal variations of the localization of tracks with more oceanic than continental tracks in winter and a more homogeneous spatial distribution in summer. These findings are consistent with previous studies on extratropical cyclones (Hoskins and Hodges, 2002; Wernli and Schwierz, 2006), the main difference being that we only consider tracks initiated between 30° N and 60° N which suppresses the representation of many Arctic cyclones in our study.

3.2.2 ETC-CPS diagrams

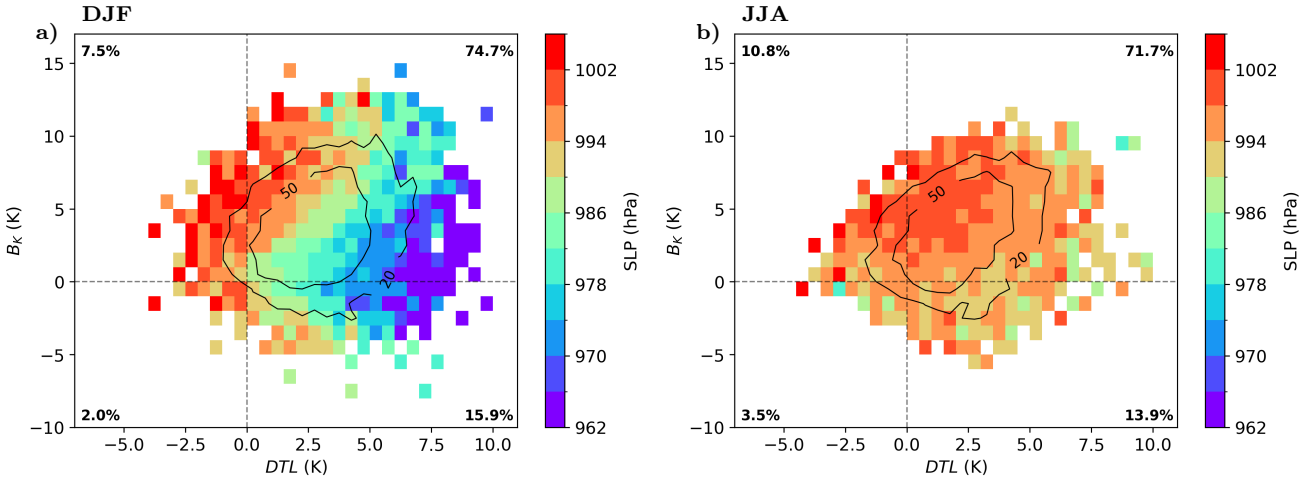

Figure 4. B_K vs. DTL diagrams for **(a)** DJF and **(b)** JJA made with track points at the time of SLP minimum only. Shading indicates the mean value of SLP in each small rectangle (hPa). Black contours indicate the density of points. Four regions are built with gray lines of value 0. The percentages of data points in each region are indicated in the corners. Rectangles with less than 3 data points were removed for visualization but not in the percentages.

Using the newly introduced ETC-CPS, we present in this section a statistical analysis of all detected cyclones in winter and summer. Figure 4 shows the 2D density distribution functions (black contours) of midlatitude cyclones in a B_K versus DTL diagram, at the time they reach their maximum intensity (i.e minimum value of the SLP) during DJF and JJA. Most cyclones are asymmetric and have warm cores during both seasons (see the large densities on the upper-right quadrants in black contours). In addition the lower the minimum SLP, the higher DTL (see shading). This is also true for both seasons but the amplitude spread is larger in winter. Hence the most intense cyclones have very pronounced warm cores whatever the season.

https://doi.org/10.5194/egusphere-2025-6174
Preprint. Discussion started: 17 December 2025

3.3 Warm- and cold-core midlatitude cyclones

In this subsection, two subsets of midlatitude cyclones are further studied: warm-core cyclones, for which DTL is positive at the time they reach their maximum intensity, and cold-core cyclones, for which DTL is negative at the time they reach their maximum intensity. Seasonal variations are also analyzed, therefore four subsets are built: warm cores DJF (91 % of all winter cyclones), cold cores DJF (9 % of all winter cyclones), warm cores JJA (86 % of all summer cyclones) and cold cores JJA (14 % of all summer cyclones). As these subsets are defined based on the value of DTL at a specific time, it is possible that the core temperature of the cyclones of each category changes during their life cycle. Composite tracks in the CPS (Fig. 5) show that warm-core cyclones stay in the warm-core part of the CPS during a large part of their life cycle. Cold-core cyclones are more characterized by a transient excursion in the cold-core half when they reach their maximum intensity. In this case, DTL is usually slightly positive before the time the cyclone reaches its minimum SLP value and stays negative thereafter, consistent with Fig. S1. Using the mean DTL value along the track or changing the radius over which DTL is calculated to 10° do not significantly affect the results.

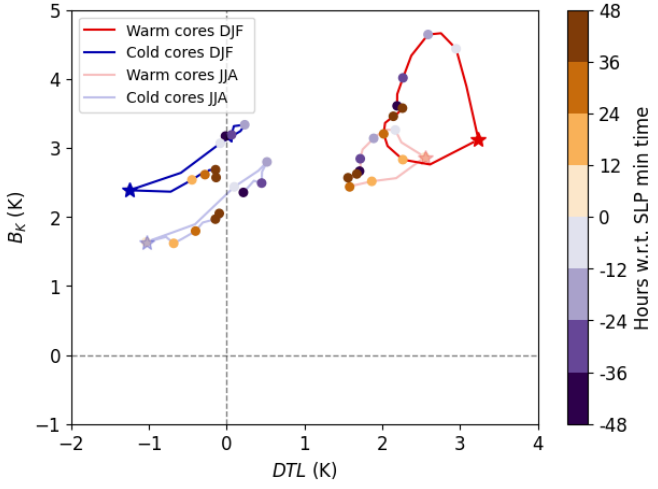

Figure 5. Mean trajectories of different subsets in the B_K vs. DTL parameter space. Red track color indicates warm-core distributions and blue track color cold-core ones. Opaque colors are associated to DJF and transparent ones to JJA. The star is the time of minimum SLP and the shading represents the lag with respect to that time.

3.3.1 Characteristics: localization, intensity, lifetime, shape

Warm-core DJF cyclones (Fig. 6a) primarily belong to the two oceanic storm tracks in the North Atlantic and North Pacific (20 cyclones per year), which are characterized by high values of 200 hPa zonal wind at their entrance. Secondary track density maxima (with about 10 cyclones per year) are also visible over continental regions, such as central North America, Russia and China, as well as over the Mediterranean Sea. Winter cold-core cyclones are mainly continental (Fig. 6c). The highest track

https://doi.org/10.5194/egusphere-2025-6174
Preprint. Discussion started: 17 December 2025

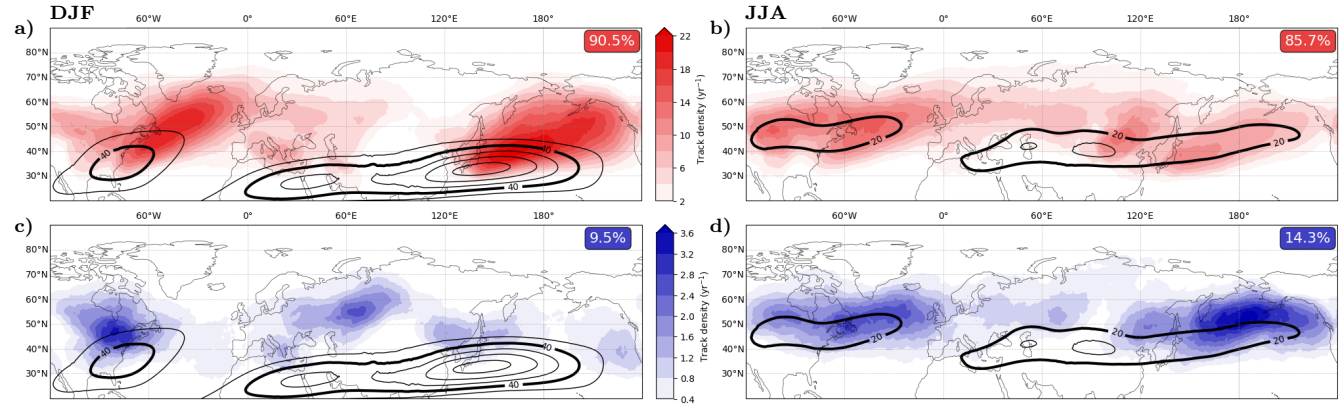

Figure 6. Same as Fig. 3 but for **(a,b)** warm-core and **(c,d)** cold-core midlatitude cyclones in **(a,c)** DJF and **(b,d)** JJA.

density regions are situated over the Great Lakes of North America and downstream of Ural mountains (2.4 cyclones per year). Three additional patches (1.2 cyclones per year) are visible in the Mediterranean Sea, in the western North Pacific near China and in the eastern North Pacific.

During JJA, warm-core and cold-core cyclones follow similar track density patterns to first order, contrarily to DJF (Fig. 6b and 6d). For both types of cyclones, the highest frequencies of occurrence are more zonally oriented and more evenly distributed between oceanic and continental regions in summer than in winter. The continental spots over northeastern America, Russia and China are relatively more active than in DJF and reach frequencies similar to the oceanic storm tracks. Regions with high-density cold-core cyclones are roughly the same as those of warm-core cyclones albeit with a slight northward shift for the former compared to the latter, in particular in the oceanic regions. The Mediterranean patch disappears for both types of cyclones.

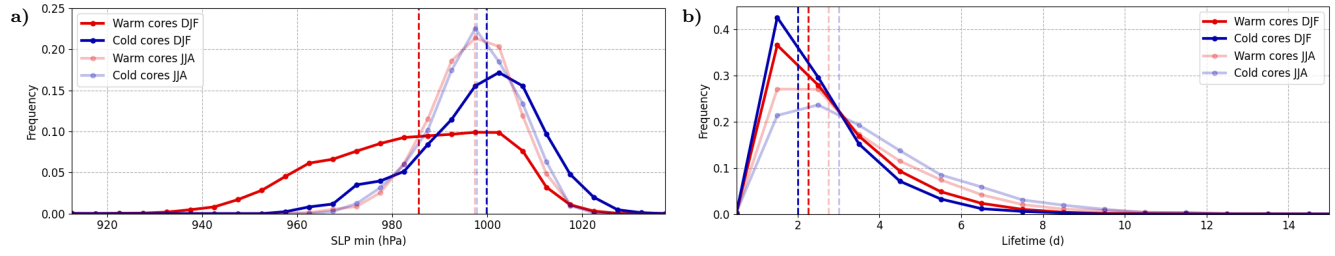

Figure 7. (a) Probability density function of SLP minimum. Red color indicates warm-core distributions and blue color cold-core ones. Opaque colors are associated to DJF and transparent ones to JJA. The dashed lines are the median values for each subset: warm cores DJF = 986 hPa, cold cores DJF = 1,000 hPa, warm cores JJA = 997 hPa, cold cores JJA = 998 hPa. **(b)** Probability density function of lifetime. The colors are the same as panel (a). The median values are: warm cores DJF = 2.5 d, cold cores DJF = 2.2 d, warm cores JJA = 3 d, cold cores JJA = 3.2 d.

https://doi.org/10.5194/egusphere-2025-6174
Preprint. Discussion started: 17 December 2025

Figure 7a shows the distribution of the minimum SLP reached by the cyclones for the four subsets. In DJF warm-core cyclones are much more intense than cold-core cyclones: their median minimum SLP is smaller by 14 hPa and their distribution is skewed toward small SLP values. In JJA warm-core cyclones are less intense and cold-core cyclones are more intense than in DJF. Both types of cyclones display the same intensity distribution in summer, centered on 998 hPa. Cyclones lifetimes are longer in JJA than in DJF (Fig. 7b). The median duration is 0.5 to 1 day higher and there is also a greater proportion of long tracks: tracks lasting more than a week represent 3 % of DJF tracks but 12 % of JJA tracks. Differences in lifetime between warm-core and cold-core cyclones are smaller than differences between seasons. Warm-core tracks are slightly longer than cold-core tracks in DJF but the ordering is reversed in JJA.

To highlight the cyclones structural differences, Fig. 8 shows a composite analysis at the time they reach their minimum SLP for the four subsets and for various variables. The first obvious result is that differences between warm-core and cold-core cyclones are higher than differences between seasons. The radial composites of temperature anomalies at 750 hPa (first row) show that warm-core cyclones exhibit a warm anomaly at the cyclone center and a cold anomaly to the southwest in DJF (Fig. 8a) and to the northwest in JJA (Fig. 8c). Such a feature is related to the westward tilt of the geopotential height anomalies Z' with height: Z' indeed decreases with height to the west of the surface cyclone but increases with height near the center and to the east of the cyclone (see Figs. 8i,j). On the contrary, for cold-core cyclones, temperature anomalies are negative over the whole cyclone area. The coldest anomalies are found near the cyclones centers and their southwest flanks (Figs. 8b,d). This is in agreement with the funnel-like shape of the geopotential anomalies of cold-core cyclones shown in Figs. 8k,l: Z' indeed decreases with height over the whole cyclone area. Consistent with the highly negative Z' values at upper levels in cold-core cyclones, the potential vorticity is high at upper levels and greater than in warm-core cyclones (compare Fig. 8i with Fig. 8k and Fig. 8j with Fig. 8l). Interestingly, although the cold-core and warm-core separation is made at 750 hPa, it holds over the largest part of the troposphere. Cold-core cyclones exhibit cold temperature anomalies between 900 hPa and 350 hPa, i.e. over almost the whole tropospheric column. Warm anomalies are found but the are confined to the boundary layer or in the stratosphere (see e.g., Fig. 8k). Warm-core cyclones are characterized by warm anomalies over the whole column with the largest anomalies near the surface (Figs. 8i,j).

Cross sections also indicate marked differences between the two categories of cyclones in terms of Eddy Kinetic Energy (EKE). Although the geopotential height anomaly minima of the warm-core and cold-core cyclones near 750 hPa are similar in JJA, the horizontal gradients of geopotential height are much larger for cold-core cyclones across the troposphere, indicating higher values of the vertically averaged EKE for the latter cyclones. In DJF the geopotential height minima are lower and the geopotential height gradients are higher for warm-core cyclones than cold-core cyclones in the lower troposphere but the opposite happens in the upper troposphere.

Radial composites of the vertical velocity ω (second row in Fig. 8) provide additional information on the differences between cold-core and warm-core cyclones. For all cyclones, an ascending zone is visible northeastward of the center and a descending zone southwestward, respectively corresponding to the warm conveyor belt (WCB) and the dry intrusion (DI) air masses. When comparing warm-core and cold-core cyclones for a given season, the ascents associated with WCB are stronger in warm-core cyclones (positive ω higher) whereas the descents associated with DI are more intense in cold-core cyclones (negative ω lower).

https://doi.org/10.5194/egusphere-2025-6174
Preprint. Discussion started: 17 December 2025

Such a result is not surprising as cold-core cyclones are dominated by upper-level anomalies from which DI descents start while warm-core cyclones are dominated by lower-level anomalies from which the WCB ascending motions start.

To summarize, warm-core cyclones are characterized by a clear vertical westward tilt of the geopotential height anomalies typical of unstable baroclinic waves (Holton, 2004) while cold-core cyclones have a funnel-like vertical structure in geopotential height anomalies. The latter structure suggests that baroclinic conversion might not be strong in the latter cyclones. This hypothesis is investigated in the following subsection.

3.3.2 Energetics

In Fig. 9, we show the seasonal 2D density distribution function in a BC versus B_K parameter space, including all tracks points for each cyclone. In both seasons, almost 80 % of them have a positive BC (black contours). The lifestage (shading) indicates that most cyclones tend to begin their life cycle with large positive values of B_K and BC and end their life cycle with values of B_K and BC close to zero. There is a minority of cyclones starting with near-zero and negative BC. These negative values are found in the upper troposphere where the geopotential height anomaly isolines are tilted eastward (not shown). The main pathway is however from high and positive values of BC to lower ones and corresponds to a typical baroclinic life cycle, during which the baroclinic conversion peaks before the cyclone maximum intensity and weakens afterwards. This is consistent with the core temperature being warm during early stages of the life cycle and close to zero at the end (Fig. S1) as baroclinic systems show a well marked westward tilt with height of geopotential height anomaly isolines which necessarily leads to a warm temperature at low levels (Holton, 2004, see e.g., Fig 6.9). The CPS diagrams shown here thus reveal that a large majority of midlatitude cyclones are driven by baroclinic processes but give no information about the distinction between cold-core and warm-core cyclones.

Figure 10 shows the time evolution of various mean (i.e. averaged over the different subsets) quantities along the tracks. The analysis of these composites is focused on the deepening of the cyclones, i.e. the part of the lagged composite before they reach their minimum SLP represented as lag 0 in the figure.

The lagged composites of SLP shown in Fig. 10a are consistent with Fig. 7a: warm-core cyclones are more intense than cold-core cyclones in DJF while they have the same intensity in JJA. It is noticeable that 48 h before the SLP reaches its minimum value, DJF warm-core cyclones already stand out by their SLP value 10 hPa lower than that of the other subsets. This can be explained by geographical and seasonal differences in climatological SLP. Warm-core winter cyclones deepen in particularly low-pressure regions, like the well-marked wintertime Icelandic and Aleutian lows (see tracks in Fig. 6a) while the other subsets develop in regions with higher climatological pressure. During the deepening phase, DJF warm-core cyclones additionally have a higher deepening rate than others as they exhibit the steepest SLP curve slope.

The vertically-averaged Eddy Total Energy (ETE) is another metric of the intensity of the synoptic systems. Its mean evolution is shown in Fig. 10b. All subsets have an ETE peak around the time of minimum SLP. The absolute values are 1.5-2 times higher in DJF than JJA. In DJF warm-core and cold-core cyclones have similar absolute values in the beginning but the slope is steeper for warm-core cyclones during the last 24 h before reaching the minimum SLP. It is consistent with the steeper slope of SLP for warm-core cyclones compared to cold-core cyclones in DJF (Fig. 10a) and confirms that warm-core cyclones

https://doi.org/10.5194/egusphere-2025-6174
Preprint. Discussion started: 17 December 2025

undergo a more explosive growth than cold-core cyclones in winter. In JJA, ETE of cold-core cyclones is larger than ETE of warm-core cyclones, but the slopes are similar for the two subsets, as are the SLP slopes.

As the baroclinic conversion rate BC plays a key role in the rate of change of ETE (see Appendix B), it is represented in Fig. 10c. All subsets show a maximum of BC around 12 h before the SLP min, which is in co-occurrence with the maximum ETE slope. In DJF the BC of warm-core cyclones is twice as large as the value of cold-core ones which is around 6.10^{-4} m^2 s^{-3}. In JJA the cold-core peak of BC occurs slightly before the warm-core one but the two peaks reach approximately the same value (4.10^{-4} m^2 s^{-3}). BC values explain thus well ETE slopes values at first order. In JJA cold-core and warm-core cyclones peaks of BC being similar is quite surprising regarding their very different vertical structure (Fig. 8). The 3D structure of BC shown in Fig. 11 provides an explanation for this apparent contradiction. Warm-core cyclones exhibit two positive peaks of BC to the west and east of the cyclone center (Fig. 11a,b), consistent with the well-marked westward tilt with height of the geopotential height anomaly contours. The composite of cold-core cyclones shows only one strong positive peak to the west and a negative peak to the east but much smaller in amplitude than the positive one, which is in agreement with the funnel-like structure of the geopotential height anomalies (Fig. 11c,d). The vertical tilt being more pronounced on the westward side, it explains the difference in amplitude between the two opposite-sign anomalies of BC in the cold-core cyclone composite. It also explains why the averaged BC is almost as large in cold-core cyclones as in warm-core cyclones in summer.

Finally the baroclinic growth rate σ, which scales the baroclinic conversion with the eddy total energy, is shown in Fig. 10d. It is also the product of the background baroclinicity and a dimensionless efficiency term that measures the efficiency of the eddies to extract energy from the background flow (Rivière and Joly, 2006b). In DJF warm-core cyclones have a higher σ than cold-core cyclones, which is not surprising because the baroclinicity on the western side of the oceanic basins where warm-core cyclones evolve is much larger than the baroclinicity in more continental regions where cold-core cyclones evolve (Fig. 6a,c). It is consistent with the DJF differences observed in BC between warm-core and cold-core cyclones in Fig. 10c. In JJA σ is also higher in warm-core cyclones, which can be explained both by the localization of their tracks – slightly closer to high baroclinicity areas (Fig. 6b,d), and by their higher efficiency due to their more pronounced westward tilted vertical structure (Fig. 11). The similar BC values between the two JJA subsets (Fig. 10c) are explained by higher ETE values in cold-core cyclones than in warm-core ones (Fig. 10b) despite their smaller σ.

To conclude, both cold-core and warm-core cyclones clearly show a pronounced baroclinic growth phase and a peak of baroclinic conversion rate before reaching their maximum intensity, but cold-core cyclones evolve in smaller baroclinicity and have a less clear westward-tilted vertical structure.

4 Conclusions

In this study, we developed a new cyclone phase space (ETC-CPS) adapted to extratropical cyclones. It keeps the simplicity of Hart (2003)'s CPS but is well adapted to investigate all kinds of cyclones including non-axisymmetric and vertically-tilted cyclones as commonly observed in extratropics. It involves three main parameters related to the core temperature, the thermal

https://doi.org/10.5194/egusphere-2025-6174
Preprint. Discussion started: 17 December 2025

asymmetry and the baroclinic growth rate. Such a CPS has been introduced to address four main questions listed in the introduction.

What is the proportion of cold-core and warm-core cyclones in midlatitudes? Most of the midlatitude cyclones have warm cores. Warm-core cyclones frequencies fluctuate between 85 % and 90 % and cold-core cyclones between 10 % and 15 %, depending on the seasons. The percentages do not change much by changing the radius used to select the environmental temperature in the newly introduced DTL diagnostic. Another important result is that the deepest cyclones are warm-core cyclones and their warm core is more pronounced at the early stage of their life. This is to be contrasted with Hart (2003)'s diagram showing a majority of cold-core cyclones but the diagnostic used in that paper, denoted to as $-VTL$, is not appropriate to detect the core temperature for baroclinic non-axisymmetric cyclones. This is mainly explained by the large-scale flow properties at midlatitudes where the highest geopotential value in the vicinity of the cyclone is found on the equatorward side of the cyclone where the temperature is the highest. In that case, the environmental temperature in Hart's diagnostic is taken at a point of highest temperature but is not representative of the temperature surrounding the cyclone. Another reason is that the temperature, which is proportional to the vertical derivative of the geopotential at each grid point following hydrostatic balance, cannot be estimated by the vertical derivative of the geopotential maximum since the maximum is not necessarily located at the same grid point for non-axisymmetric cyclones.

Are occluded cyclones cold-core or warm-core cyclones? Although our analysis does not systematically separate between occluded and warm-seclusion cyclones, we analyzed two cyclones representative of these two categories. As expected, the warm-seclusion cyclone has a well-defined warm core but the occluded cyclone also has a warm core even though less well marked. Since we show that deep cyclones have generally warm cores, it is thus very unlikely to encounter a deep occluded cyclone with a cold core.

What are the main characteristics of cold-core and warm-core cyclones? Both types of cyclones are characterized by strong thermal asymmetry at the early stage of their life cycle and more neutral thermal asymmetry at the later stage. Cold-core cyclones reach their coldest core temperature at the later stage of their life cycle and tend to have a slightly warm core temperature at the early stage when they grow baroclinically. In winter warm-core cyclones are intense and develop over oceanic storm tracks whereas cold-core cyclones are weaker in intensity and develop more over continental regions. In summer warm-core and cold-core cyclones roughly have the same intensity and develop in the same geographical areas, mainly over the two oceanic storm tracks but also over some continental regions.

How different are the main processes leading to the formation of cold-core and warm-core cyclones? Both types of cyclones undergo a well-marked baroclinic phase during the main deepening phase leading to the SLP minimum. But their vertical structures differ a lot during that phase. Warm-core cyclones exhibit a clear vertical westward tilt of the geopotential height anomaly contours as in the classical picture of a developing synoptic disturbance or baroclinic unstable mode (Holton, 2004, see e.g., Figs. 6.9 and 8.10). Cold-core cyclones have a funnel-like vertical structure in the anomalous geopotential height field leaning more westward than eastward which makes them also grow baroclinically but with a non-standard baroclinic structure. In winter most cold-core cyclones are initiated on the downstream side of mountain ranges and their tracks are not necessarily close to regions of high baroclinicity whereas warm-core cyclones mainly form and deepen in regions of high baroclinicity.

https://doi.org/10.5194/egusphere-2025-6174
Preprint. Discussion started: 17 December 2025

This difference largely explains why baroclinic conversion rate is much greater for warm-core cyclones than cold-core ones in winter. In contrast, in summer, track densities of the two categories of cyclones are closer to each other and they have similar amplitude of baroclinic conversion rate, albeit somewhat weaker for cold-core cyclones which evolve slightly further north of the main baroclinicity region compared to warm-core cyclones.

To our knowledge, the present study is the first one to systematically detect cold-core and warm-core cyclones in midlatitudes and detail their main differences. Several aspects need to be further investigated in the future. It is not clear yet why cold-core cyclones are closely related to mountain ranges in winter and not so much in summer. Although we do show that baroclinic growth is a key process of the main deepening phase of both cyclones, other energetic aspects need to be further analyzed, in particular diabatic generation terms. Figure S2 shows the diabatic generation term in summer as a function of time, together with BC (see definitions in Appendix B). The diabatic generation rate is smaller than the baroclinic conversion rate for both summer subsets but we do see even smaller values for cold-core cyclones than warm-core cyclones. Such a result is consistent with weaker ascending motion in cold-core cyclones which probably leads to less strong latent heating in their WCB. However a detailed energy budget would be required to further elucidate why the deepening of cold-core cyclones is as large as warm-core cyclones in summer.

Despite their smaller percentage of frequencies of occurrence, cold-core cyclones are most intriguing because their structure do not seem consistent with the classic baroclinic growth models. Analyzing their development more in detail would surely be of interest. In particular they might be linked to tropopause polar vortices (TPVs) that are meso- to synoptic-scale tropopause coherent cyclonic vortices frequently observed in polar regions (Cavallo and Hakim, 2010). Our composites of cold-core cyclones exhibit intense cyclonic vortices marked by high PV that resemble TPVs. Since TPVs are known to have incursions in the midlatitudes where they may initiate midlatitude cyclogenesis (Schäfler et al., 2018), it is likely that many cold-core cyclones are formed during baroclinic interaction with TPVs.

Another perspective would be to adopt a Lagrangian approach to study the differences between cold-core and warm-core cyclones. Cold-core cyclones probably have a stronger dry intrusion and a weaker warm conveyor belt following our vertical velocity composites but this needs to be confirmed by a proper Lagrangian analysis. Since the 3D structure of cold-core cyclones is largely different from warm-core cyclones, one can expect very different Lagrangian trajectories.

Cold-core cyclones are probably more frequent in the Arctic than in midlatitudes as illustrated by many case studies (Aizawa and Tanaka, 2016; Croad et al., 2023a; Rivière et al., 2024) and the summertime statistical analysis of Croad et al. (2023b). More statistical studies need to be done in the future to investigate more deeply the processes involved in Arctic cyclones during both summer and winter. Finally another outcome of the present study would be to analyze cold-core and warm-core cyclones representation in climate models. Our simple ETC-CPS diagrams offer an opportunity to investigate these different cyclones in the models.

https://doi.org/10.5194/egusphere-2025-6174
Preprint. Discussion started: 17 December 2025

Appendix A: Anomaly computations

An example of the anomaly computation is given here with T, it applies the same for Z. The anomaly of T is defined as:

$$T' = T - \overline{T} \tag{A1}$$

$$= T - \left(\langle T \rangle + \langle \nabla T \rangle \cdot (\mathbf{x} - \mathbf{x}_C)\right) \tag{A2}$$

$$= T - \langle T \rangle - \begin{pmatrix} \left\langle \frac{\partial T}{\partial x} \right\rangle \\ \left\langle \frac{\partial T}{\partial y} \right\rangle \end{pmatrix} \cdot \begin{pmatrix} x - x_C \\ y - y_C \end{pmatrix} \tag{A3}$$

The brackets stand for an azimuthal weighted mean on a 10°-circle. (x, y) is a zonal-meridional basis defined on the sphere. The subscript $_C$ refers to the center of the cyclone.

The coordinates x and y can be computed with longitude λ and latitude ϕ as follows:

$$\begin{cases} x - x_C = a\cos\phi(\lambda - \lambda_C) \\ y - y_C = a(\phi - \phi_C) \end{cases} \tag{A4}$$

As for the derivatives, let us first express the derivatives relative to (x, y) as a function of the derivatives relative to (λ, ϕ):

$$\begin{cases} \frac{\partial T}{\partial x} = \frac{\partial T}{\partial \phi}\frac{\partial \phi}{\partial x} + \frac{\partial T}{\partial \lambda}\frac{\partial \lambda}{\partial x} = \frac{1}{a\cos\phi}\frac{\partial T}{\partial \lambda} \\ \frac{\partial T}{\partial y} = \frac{\partial T}{\partial \phi}\frac{\partial \phi}{\partial y} + \frac{\partial T}{\partial \lambda}\frac{\partial \lambda}{\partial y} = \frac{1}{a}\frac{\partial T}{\partial \phi} \end{cases} \tag{A5}$$

The snapshots provided by TempestExtremes' code are on a plane corresponding to a stereographic projection around a central point (λ_0, ϕ_0) (in our case (λ_C, ϕ_C)). We define the Cartesian basis (X, Y) oriented eastward and northward. The derivatives of T with respect to the (λ, ϕ) basis can be expressed as follows:

$$\begin{cases} \frac{\partial T}{\partial \lambda} = \frac{\partial T}{\partial X}\frac{\partial X}{\partial \lambda} + \frac{\partial T}{\partial Y}\frac{\partial Y}{\partial \lambda} \\ \frac{\partial T}{\partial \phi} = \frac{\partial T}{\partial X}\frac{\partial X}{\partial \phi} + \frac{\partial T}{\partial Y}\frac{\partial Y}{\partial \phi} \end{cases} \tag{A6}$$

The derivatives of X and Y relatively to λ and ϕ can be computed with Ullrich et al. (2021)'s Appendix A formulas, more precisely (A2) and (A3). Note that there is a factor 2 missing in (A1) in the paper (but not in TempestExtremes' code): the correct formula is $K = 2[1 + \sin\phi\sin\phi_0 + \cos\phi\cos\phi_0\cos(\lambda - \lambda_0)]^{-1}$. With this, the following derivatives can be analytically computed:

$$\begin{cases} \frac{\partial X}{\partial \lambda} = \cos\phi\frac{\partial Y}{\partial \phi} = \frac{2\cos\phi\,(\cos\phi\cos\phi_0 + \cos(\lambda - \lambda_0)\,(1 + \sin\phi\sin\phi_0))}{D^2} \\ \frac{\partial Y}{\partial \lambda} = -\cos\phi\frac{\partial X}{\partial \phi} = \frac{2\cos\phi\sin(\lambda - \lambda_0)(\sin\phi_0 + \sin\phi)}{D^2} \end{cases}, \tag{A7}$$

with $D = 1 + \sin(\phi)\sin(\phi_0) + \cos(\phi)\cos(\phi_0)\cos(\lambda - \lambda_0)$.

https://doi.org/10.5194/egusphere-2025-6174
Preprint. Discussion started: 17 December 2025

If the output basis of TempestExtremes' snapshot is (X, Y), the computation of the derivatives of T is simple. In our case, the output is in a radial basis (r, ϑ) so the derivatives are computed by a projection from this basis (r, ϑ) on the basis (X, Y):

$$\nabla T = \frac{\partial T}{\partial X}\mathbf{e_X} + \frac{\partial T}{\partial Y}\mathbf{e_Y} = \frac{\partial T}{\partial r}\mathbf{e_r} + \frac{1}{r}\frac{\partial T}{\partial \vartheta}\mathbf{e}_\vartheta \tag{A8}$$

With geometrical considerations, we have: $\mathbf{e_X} = \cos\vartheta\mathbf{e_r} - \sin\vartheta\mathbf{e}_\vartheta$ and $\mathbf{e_Y} = \sin\vartheta\mathbf{e_r} + \cos\vartheta\mathbf{e}_\vartheta$, so we can write:

$$\begin{cases} \dfrac{\partial T}{\partial X} = \nabla T.\mathbf{e_X} = \dfrac{\partial T}{\partial r}\cos\vartheta - \dfrac{1}{r}\dfrac{\partial T}{\partial \vartheta}\sin\vartheta \\ \dfrac{\partial T}{\partial Y} = \nabla T.\mathbf{e_Y} = \dfrac{\partial T}{\partial r}\sin\vartheta + \dfrac{1}{r}\dfrac{\partial T}{\partial \vartheta}\cos\vartheta \end{cases} \tag{A9}$$

To sum up, to compute the derivatives of T with respect to (x, y), we first compute the derivatives of T with respect to (r, ϑ) and then use equations (A6), (A7) and (A9).

Appendix B: Eddy energy budget

To keep the decomposition between the background flow and the synoptic eddies as simple as possible, the background winds are defined as the areal averages of the winds over a circle centred at the cyclone center and a radius of 10°. Since we want the background flow to satisfy the geostrophic and thermal wind balances, the background geopotential and temperature should have uniform horizontal gradients inside the circle. This is the reason why different spatial operators are applied to define the background winds and the background temperature and geopotential. Accordingly the areal average over the circle, denoted as $\langle x \rangle$, is applied to the momentum equation to get the Eddy Kinetic Energy (EKE) equation and the operator $\overline{x} = \langle x \rangle + \langle \nabla x \rangle \cdot \mathbf{x} =$ is applied to the thermodynamical equation to get the Eddy Potential Energy (EPE) equation. Primes and seconds define the following operators: $x' = x - \langle x \rangle$ and $x'' = x - \overline{x} = x - \langle x \rangle - \langle \nabla x \rangle \cdot \mathbf{x}$.

B1 EKE budget

The eddy kinetic energy budget is derived from the following momentum equation:

$$\frac{\partial \mathbf{u}}{\partial t} = -\mathbf{u}_3 \cdot \nabla_3 \mathbf{u} - f\mathbf{k} \times \mathbf{u} - \nabla\phi + \mathbf{F}, \tag{B1}$$

where $\mathbf{F}$ denote frictional processes, ∇_3 is the three-dimensional gradient operator, ∇ is the horizontal gradient operator, $\mathbf{u}_3$ is the three-dimensional wind velocity and $\mathbf{u}$ is the horizontal wind velocity. By applying $\langle\ \rangle$ to Eq. (B1), one gets:

$$\frac{\partial \langle \mathbf{u} \rangle}{\partial t} = -\langle \mathbf{u}_3 \cdot \nabla_3 \mathbf{u} \rangle - \langle f\mathbf{k} \times \mathbf{u} \rangle - \langle \nabla\phi \rangle + \langle \mathbf{F} \rangle \tag{B2}$$

By subtracting Eq. (B2) to Eq. (B1), it gives:

$$\begin{aligned} \frac{\partial \mathbf{u}'}{\partial t} &= -\mathbf{u}_3 \cdot \nabla_3 \mathbf{u} + \langle \mathbf{u}_3 \cdot \nabla_3 \mathbf{u} \rangle - f\mathbf{k} \times \mathbf{u} + \langle f\mathbf{k} \times \mathbf{u} \rangle - \nabla\phi + \langle \nabla\phi \rangle + \mathbf{F} - \langle \mathbf{F} \rangle \\ &= -\left(\mathbf{u}_3 \cdot \nabla_3 \mathbf{u} - \langle \mathbf{u}_3 \cdot \nabla_3 \mathbf{u} \rangle\right) - \left(f\mathbf{k} \times \mathbf{u} - \langle f\mathbf{k} \times \mathbf{u} \rangle\right) - \left(\nabla\phi - \nabla\left(\langle\phi\rangle + \langle\nabla\phi\rangle \cdot \mathbf{x}\right)\right) + \left(\mathbf{F} - \langle \mathbf{F} \rangle\right) \\ &\simeq -\left(\mathbf{u}_3 \cdot \nabla_3 \mathbf{u}\right)' - f\mathbf{k} \times \mathbf{u}' - \nabla\phi'' + \mathbf{F}' \end{aligned} \tag{B3}$$

https://doi.org/10.5194/egusphere-2025-6174
Preprint. Discussion started: 17 December 2025

By multiplying it by $\mathbf{u}'$, one gets:

$$\frac{\partial EKE}{\partial t} = \frac{\partial}{\partial t}\left(\frac{1}{2}\mathbf{u}'^2\right) = -\mathbf{u}' \cdot (\mathbf{u}_3 \cdot \nabla_3 \mathbf{u})' - \mathbf{u}' \cdot \nabla \phi'' + \mathbf{u}' \cdot \mathbf{F}' \tag{B4}$$

The first term is an advection term, then comes a pressure work term – which includes the so-called baroclinic conversion rate from eddy potential energy to eddy kinetic energy (or also called internal baroclinic conversion rate) – and finally a friction term similar to the decomposition based on time filtering (Schemm and Rivière, 2019).

B2 EPE budget

The eddy potential energy budget is derived from the thermodynamical equation:

$$\frac{\partial \theta}{\partial t} = -\mathbf{u}_3 \cdot \nabla_3 \theta + Q, \tag{B5}$$

where θ is potential temperature and Q the diabatic heating rate. By applying the overbar operator to the previous equation, one gets:

$$\frac{\partial \overline{\theta}}{\partial t} = -\overline{(\mathbf{u}_3 \cdot \nabla_3 \theta)} + \overline{Q} \tag{B6}$$

The subtraction of Eq. (B6) to Eq. (B5) gives:

$$\frac{\partial \theta''}{\partial t} = -\left(\mathbf{u}_3 \cdot \nabla_3 \theta\right)'' + Q'' \tag{B7}$$

By multiplying it by θ''/S, one gets:

$$\frac{\partial EPE}{\partial t} = \frac{\partial}{\partial t}\left(\frac{1}{2}\frac{\theta''^2}{S}\right) = -\frac{\theta''}{S}\left(\mathbf{u} \cdot \nabla \theta\right)'' + \frac{\theta'' Q''}{S}, \tag{B8}$$

where $S = -\frac{1}{h}\frac{\partial \langle \theta \rangle}{\partial p}$ ($\mathrm{K^2\ s^2\ m^{-2}}$) is the static stability in pressure coordinates, with $h = \frac{R}{p}\left(\frac{p}{p_0}\right)^{\kappa}$ ($\mathrm{m^3\ kg^{-1}\ K^{-1}}$).

The advection term (first term) can be decomposed:

$$\begin{aligned}
-\frac{\theta''}{S}\left(\mathbf{u}_3 \cdot \nabla_3 \theta\right)'' &= -\frac{\theta''}{S}\left(\mathbf{u}_3 \cdot \nabla_3 \theta - \overline{\mathbf{u}_3 \cdot \nabla_3 \theta}\right) \\
&= -\frac{\theta''}{S}\left(\mathbf{u}_3 \cdot \nabla_3 \left(\theta'' + \overline{\theta}\right)\right) + \frac{\theta''}{S}\overline{\mathbf{u}_3 \cdot \nabla_3 \theta} \\
&= -\frac{\theta''}{S}\left(\mathbf{u}_3 \cdot \nabla_3 \theta''\right) - \frac{\theta''}{S}\left(\mathbf{u}_3 \cdot \nabla_3 \overline{\theta}\right) + \frac{\theta''}{S}\overline{\mathbf{u}_3 \cdot \nabla_3 \theta} \\
&= -\nabla \cdot \left(\mathbf{u}\, EPE\right) - \frac{1}{S}\frac{\partial}{\partial p}\left(\omega \frac{\theta''^2}{2}\right) - \frac{\theta''}{S}\left(\mathbf{u}' \cdot \nabla \overline{\theta}\right) - \frac{\theta'' \omega'}{S}\frac{\partial \overline{\theta}}{\partial p} - \frac{\theta''}{S}\left(\langle \mathbf{u}_3 \rangle \cdot \nabla_3 \overline{\theta} - \overline{\mathbf{u}_3 \cdot \nabla_3 \theta}\right)
\end{aligned} \tag{B9}$$

The first two terms on the r.h.s. of the equation correspond to the three-dimensional advection of EPE, the third term to the baroclinic conversion rate from background potential energy to eddy potential energy (also called external baroclinic conversion rate and denoted BC in the whole paper), the fourth term to minus the internal baroclinic conversion rate from eddy potential energy to eddy kinetic energy and the last one is a residual term. Here again the eddy potential energy equation is similar to that based on time filtering (Schemm and Rivière, 2019).

https://doi.org/10.5194/egusphere-2025-6174
Preprint. Discussion started: 17 December 2025

When adding the eddy potential energy and eddy kinetic energy equations to get the eddy total energy equation, the internal baroclinic conversion rate disappears and the external baroclinic conversion rate $BC = -\frac{\theta''}{S}\left(\mathbf{u}' \cdot \nabla\overline{\theta}\right)$ remains and is the main source of growth for baroclinic disturbances together with the diabatic generation term $DG = \frac{\theta'' Q''}{S}$. For simplicity purposes, θ'' is replaced by θ' and the geopotential height anomaly Z'' by Z' in the main text.

Author contributions. MB, GR and SF did the conceptualization and investigation; MB did the figures and wrote the article draft; MB, GR and SF reviewed and edited the manuscript.

Competing interests. The authors declare that they have no conflict of interest.

Acknowledgements. This work was supported by an École Normale Supérieure – Paris Sciences et Lettres PhD grant and by two CNRS projects funded via its program INSU-LEFE: CYCLONICE and DEMONIAC. The authors kindly thank Stella Bourdin for her CPyS Python package (https://github.com/stella-bourdin/CPyS) that allows the computation of some parameters in a very easy way.

https://doi.org/10.5194/egusphere-2025-6174
Preprint. Discussion started: 17 December 2025

References

Aizawa, T. and Tanaka, H. L.: Axisymmetric structure of the long lasting summer Arctic cyclones, Polar Science, 10, 192–198, https://doi.org/10.1016/j.polar.2016.02.002, 2016.

Azad, R. and Sorteberg, A.: A diagnosis of warm-core and cold-core extratropical cyclone development using the Zwack–Okossi equation, Atmospheric Science Letters, 10, 220–225, https://doi.org/10.1002/asl.244, 2009.

Bjerknes, J. and Solberg, H.: Life cycle of cyclones and the polar front theory of atmospheric circulation, Cammermeyers Bogh., 1922.

Cai, M. and Mak, M.: On the basic dynamics of regional cyclogenesis, Journal of Atmospheric Sciences, 47, 1417–1442, 1990.

Catto, J. L.: Extratropical cyclone classification and its use in climate studies, Reviews of Geophysics, 54, 486–520, https://doi.org/10.1002/2016RG000519, 2016.

Catto, J. L., Jakob, C., Berry, G., and Nicholls, N.: Relating global precipitation to atmospheric fronts, Geophysical Research Letters, 39, https://doi.org/10.1029/2012GL051736, 2012.

Cavallo, S. M. and Hakim, G. J.: Composite Structure of Tropopause Polar Cyclones, Monthly Weather Review, 138, 3840–3857, https://doi.org/10.1175/2010MWR3371.1, publisher: American Meteorological Society Section: Monthly Weather Review, 2010.

Chang, E. K. M., Lee, S., and Swanson, K. L.: Storm track dynamics, Journal of Climate, 15, 2163–2183, 2002.

Charney, J. G.: The dynamics of long waves in a baroclinic westerly current, Journal of Atmospheric Sciences, 4, 136–162, 1947.

Croad, H. L., Methven, J., Harvey, B., Keeley, S. P. E., and Volonté, A.: The role of boundary layer processes in summer-time Arctic cyclones, Weather and Climate Dynamics, 4, 617–638, https://doi.org/10.5194/wcd-4-617-2023, 2023a.

Croad, H. L., Methven, J., Harvey, B., Keeley, S. P. E., Volonté, A., and Hodges, K. I.: A Climatology of Summer-Time Arctic Cyclones Using a Modified Phase Space, Geophysical Research Letters, 50, https://doi.org/10.1029/2023GL105993, 2023b.

Dacre, H. F., Hawcroft, M. K., Stringer, M. A., and Hodges, K. I.: An extratropical cyclone atlas: a tool for illustrating cyclone structure and evolution characteristics, Bulletin of the American Meteorological Society, 93, 1497–1502, https://doi.org/10.1175/BAMS-D-11-00164.1, 2012.

Eady, E. T.: Long waves and cyclone waves, Tellus, 1, 33–52, https://doi.org/10.3402/tellusa.v1i3.8507, 1949.

Emanuel, K.: Tropical cyclones, Annual Review of Earth and Planetary Sciences, 31, 75–104, https://doi.org/10.1146/annurev.earth.31.100901.141259, 2003.

Emanuel, K., Alberti, T., Bourdin, S., Camargo, S. J., Faranda, D., Flaounas, E., Gonzalez-Aleman, J. J., Lee, C.-Y., Miglietta, M. M., Pasquero, C., Portal, A., Ramsay, H., Reale, M., and Romero, R.: CYCLOPs: a Unified Framework for Surface Flux-Driven Cyclones Outside the Tropics, Weather and Climate Dynamics, 6, 901–926, https://doi.org/10.5194/wcd-6-901-2025, publisher: Copernicus GmbH, 2025.

Fink, A. H., Brücher, T., Ermert, V., Krüger, A., and Pinto, J. G.: The European storm Kyrill in January 2007: synoptic evolution, meteorological impacts and some considerations with respect to climate change, Natural Hazards and Earth System Sciences, 9, 405–423, https://doi.org/10.5194/nhess-9-405-2009, 2009.

Flaounas, E., Davolio, S., Raveh-Rubin, S., Pantillon, F., Miglietta, M. M., Gaertner, M. A., Hatzaki, M., Homar, V., Khodayar, S., Korres, G., et al.: Mediterranean cyclones: current knowledge and open questions on dynamics, prediction, climatology and impacts, Weather and Climate Dynamics, 3, 173–208, https://doi.org/10.5194/wcd-3-173-2022, 2022.

Gray, S. L. and Volonté, A.: Extreme low-level wind jets in Storm Ciarán, Weather, 79, 384–389, https://doi.org/10.1002/wea.7620, _eprint: https://rmets.onlinelibrary.wiley.com/doi/pdf/10.1002/wea.7620, 2024.

https://doi.org/10.5194/egusphere-2025-6174
Preprint. Discussion started: 17 December 2025

Gray, S. L., Hodges, K. I., Vautrey, J. L., and Methven, J.: The role of tropopause polar vortices in the intensification of summer Arctic cyclones, Weather and Climate Dynamics, 2, 1303–1324, https://doi.org/10.5194/wcd-2-1303-2021, publisher: Copernicus GmbH, 2021.

Hart, R.: A Cyclone Phase Space Derived from Thermal Wind and Thermal Asymmetry, Monthly Weather Review, 131, 585–616, 2003.

Hersbach, H., Bell, B., Berrisford, P., Hirahara, S., Horányi, A., Muñoz-Sabater, J., Nicolas, J., Peubey, C., Radu, R., Schepers, D., et al.: The ERA5 global reanalysis, Quarterly Journal of the Royal Meteorological Society, 146, 1999–2049, https://doi.org/10.1002/qj.3803, 2020.

Holton, J.: An introduction to dynamic meteorology, 4th Edition., Elsevier Academic Press, international Geophyscis Series, Vol. 88, 535 pp, 2004.

Hoskins, B. J. and Hodges, K. I.: New Perspectives on the Northern Hemisphere Winter Storm Tracks, Journal of the Atmospheric Sciences, 59, 1041–1061, https://doi.org/10.1175/1520-0469(2002)059<1041:NPOTNH>2.0.CO;2, publisher: American Meteorological Society Section: Journal of the Atmospheric Sciences, 2002.

Lindzen, R. S. and Farrell, B.: A simple approximate result for the maximum growth rate of baroclinic instabilities, Journal of the Atmospheric Sciences, 37, 1648–1654, 1980.

Neu, U., Akperov, M. G., Bellenbaum, N., Benestad, R., Blender, R., Caballero, R., Cocozza, A., Dacre, H. F., Feng, Y., Fraedrich, K., Grieger, J., Gulev, S., Hanley, J., Hewson, T., Inatsu, M., Keay, K., Kew, S. F., Kindem, I., Leckebusch, G. C., Liberato, M. L. R., Lionello, P., Mokhov, I. I., Pinto, J. G., Raible, C. C., Reale, M., Rudeva, I., Schuster, M., Simmonds, I., Sinclair, M., Sprenger, M., Tilinina, N. D., Trigo, I. F., Ulbrich, S., Ulbrich, U., Wang, X. L., and Wernli, H.: IMILAST - A community effort to intercompare extratropical cyclone detection and tracking algorithms, American Meteorological Society, pp. 529–547, https://doi.org/10.1175/BAMS-D-11-00154.1, 2013.

Peixoto, J. P. and Oort, A. H.: Physics of climate, New York, NY (United States); American Institute of Physics, 1992.

Pinto, J. G., Spangehl, T., Ulbrich, U., and Speth, P.: Sensitivities of a cyclone detection and tracking algorithm: individual tracks and climatology, Meteorologische Zeitschrift, 14, 823–838, https://doi.org/10.1127/0941-2948/2005/0068, 2005.

Priestley, M. D. K. and Catto, J. L.: Future changes in the extratropical storm tracks and cyclone intensity, wind speed, and structure, Weather and Climate Dynamics, 3, 337–360, https://doi.org/10.5194/wcd-3-337-2022, publisher: Copernicus GmbH, 2022.

Rivière, G. and Joly, A.: Role of the low-frequency deformation field on the explosive growth of extratropical cyclones at the jet exit. Part I: Barotropic critical region, Journal of the atmospheric sciences, 63, 1965–1981, https://doi.org/10.1175/JAS3728.1, 2006a.

Rivière, G. and Joly, A.: Role of the low-frequency deformation field on the explosive growth of extratropical cyclones at the jet exit. Part II: Baroclinic critical region, Journal of the atmospheric sciences, 63, 1982–1995, https://doi.org/10.1175/JAS3729.1, 2006b.

Rivière, G., Arbogast, P., and Joly, A.: Eddy kinetic energy redistribution within idealized extratropical cyclones using a two-layer quasi-geostrophic model, Quarterly Journal of the Royal Meteorological Society, 141, 207–223, https://doi.org/10.1002/qj.2350, 2015.

Rivière, G., Delanoë, J., Doyle, J. D., Methven, J., Barrell, C., Fearon, M., Gray, S., Johnson, A., Jourdan, O., Lachlan-Cope, T., et al.: The THINICE field campaign: Interactions between arctic cyclones, tropopause polar vortices, clouds, and sea ice in summer, Bulletin of the American Meteorological Society, 105, E2330–E2354, https://doi.org/10.1175/BAMS-D-23-0143.1, 2024.

Schär, C.: Orographic Effects: Lee Cyclogenesis, Encyclopedia of Atmospheric Sciences, 2nd Edition, 4, 103–113, https://doi.org/10.1016/B978-0-12-382225-3.00290-5, 2003.

Schemm, S. and Rivière, G.: On the efficiency of baroclinic eddy growth and how it reduces the North Pacific storm-track intensity in midwinter, Journal of Climate, 32, 8373–8398, https://doi.org/10.1175/JCLI-D-19-0115., 2019.

Schultz, D. M., Keyser, D., and Bosart, L. F.: The Effect of Large-Scale Flow on Low-Level Frontal Structure and Evolution in Midlatitude Cyclones, Monthly Weather Review, 126, 1767–1791, https://doi.org/10.1175/1520-0493(1998)126<1767:TEOLSF>2.0.CO;2, publisher: American Meteorological Society Section: Monthly Weather Review, 1998.

https://doi.org/10.5194/egusphere-2025-6174
Preprint. Discussion started: 17 December 2025

Schäfler, A., Craig, G., Wernli, H., Arbogast, P., Doyle, J. D., McTaggart-Cowan, R., Methven, J., Rivière, G., Ament, F., Boettcher, M., Bramberger, M., Cazenave, Q., Cotton, R., Crewell, S., Delanoë, J., Dörnbrack, A., Ehrlich, A., Ewald, F., Fix, A., Grams, C. M., Gray, S. L., Grob, H., Groß, S., Hagen, M., Harvey, B., Hirsch, L., Jacob, M., Kölling, T., Konow, H., Lemmerz, C., Lux, O., Magnusson, L., Mayer, B., Mech, M., Moore, R., Pelon, J., Quinting, J., Rahm, S., Rapp, M., Rautenhaus, M., Reitebuch, O., Reynolds, C. A., Sodemann, H., Spengler, T., Vaughan, G., Wendisch, M., Wirth, M., Witschas, B., Wolf, K., and Zinner, T.: The North Atlantic Waveguide and Downstream Impact Experiment, Bulletin of the American Meteorological Society, 99, 1607–1637, https://doi.org/10.1175/BAMS-D-17-0003.1, publisher: American Meteorological Society Section: Bulletin of the American Meteorological Society, 2018.

Shapiro, M. A. and Keyser, D.: Fronts, jet streams and the tropopause, Springer, 1990.

Simmons, A. J. and Hoskins, B. J.: The life cycles of some nonlinear baroclinic waves, Journal of Atmospheric Sciences, 35, 414–432, 1978.

Ulbrich, U., Leckebusch, G. C., and Pinto, J. G.: Extra-tropical cyclones in the present and future climate: a review, Theoretical and applied climatology, 96, 117–131, https://doi.org/10.1007/s00704-008-0083-8, 2009.

Ullrich, P. A. and Zarzycki, C. M.: TempestExtremes: a framework for scale-insensitive pointwise feature tracking on unstructured grids, Geoscientific Model Development, 10, 1069–1090, https://doi.org/10.5194/gmd-10-1069-2017, 2017.

Ullrich, P. A., Zarzycki, C. M., McClenny, E. E., Pinheiro, M. C., Stansfield, A. M., and Reed, K. A.: TempestExtremes v2.1: a community framework for feature detection, tracking, and analysis in large datasets, Geoscientific Model Development, 14, 5023–5048, https://doi.org/10.5194/gmd-14-5023-2021, 2021.

Volonté, A. and Riboldi, J.: The origins of Storm Ciarán: From diabatic Rossby wave to warm-seclusion cyclone with a sting jet, Weather, 79, 390–396, https://doi.org/10.1002/wea.7632, 2024.

Wang, Z., Yang, M., Walsh, J. E., Rauber, R. M., and Peng, M.: A Diagnostic Analysis of the Mechanisms for Arctic Cyclones Intensity Evolution, Journal of the Atmospheric Sciences, 81, 1383–1399, https://doi.org/10.1175/JAS-D-23-0130.1, 2024.

Wernli, H. and Schwierz, C.: Surface Cyclones in the ERA-40 Dataset (1958–2001). Part I: Novel Identification Method and Global Climatology, Journal of the Atmospheric Sciences, 63, 2486–2507, https://doi.org/10.1175/JAS3766.1, publisher: American Meteorological Society Section: Journal of the Atmospheric Sciences, 2006.

https://doi.org/10.5194/egusphere-2025-6174
Preprint. Discussion started: 17 December 2025

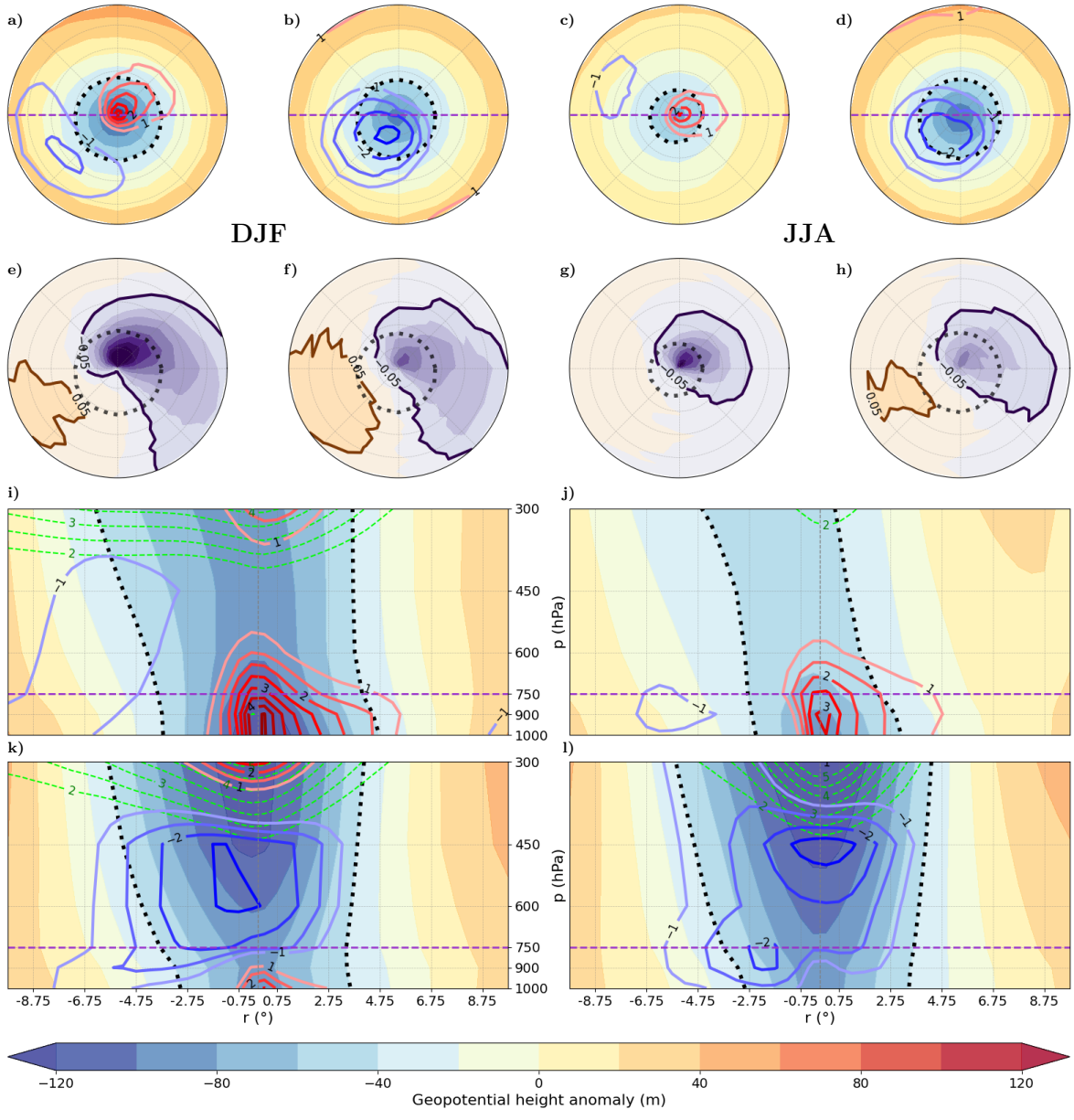

Figure 8. Radial **(a–h)** and vertical **(i–l)** composites of different subsets at SLP min time. Radial composites are made at 750 hPa. Vertical composites are made on the cross section represented by the dashed purple line in panels (a–d). **(a,e,i)** DJF warm cores. **(b,f,k)** DJF cold cores. **(c,g,j)** JJA warm cores. **(d,h,l)** JJA cold cores. In (a–d) and (i–l) panels, shading represents the geopotential height anomaly contours, the -40 m value being highlighted by a dotted black line, and red-blue contours represent the temperature anomaly in K. In **(e-h)** panels, shading represents the vertical velocity ω with 0.05 Pa s^{-1} contours, 0.05 and -0.05 Pa s^{-1} being highlighted by bold contours. In (i-l) panels, dashed green contours represent the potential vorticity (every 1 PVU starting at 2 PVU). See Appendix A for more details on the computation of geopotential height and temperature anomalies.

https://doi.org/10.5194/egusphere-2025-6174
Preprint. Discussion started: 17 December 2025

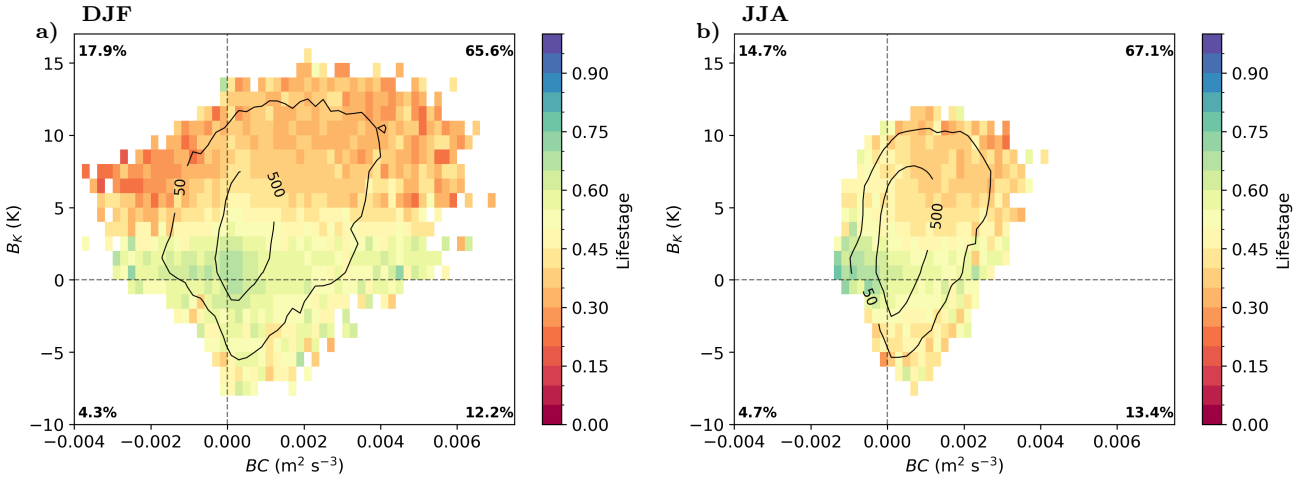

Figure 9. B_K vs. BC diagrams for **(a)** DJF and **(b)** JJA. The diagrams are made with all track points. Shading indicates the mean lifestage in each small square. Black contours indicate the density of points. Four regions are built with gray lines of value 0. The percentages of data points in each region are indicated in the corners. Rectangles with less than 10 data points were removed for visualization but not in the percentages.

https://doi.org/10.5194/egusphere-2025-6174
Preprint. Discussion started: 17 December 2025

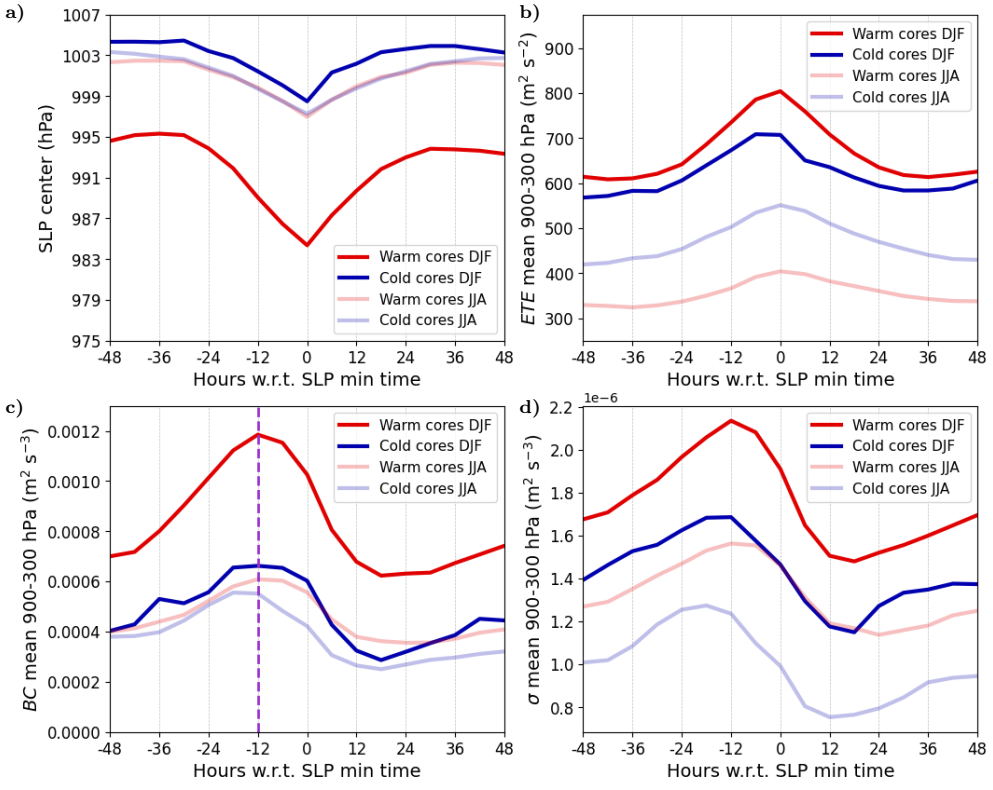

Figure 10. Lagged composites of **(a)** SLP of the center, **(b)** mean ETE on a 10°-radius circle and on the layers between 900 and 300 hPa, **(c)** mean BC on a 10°-radius circle and on the layers between 900 and 300 hPa, **(d)** mean σ on a 10°-radius circle and on the layers between 900 and 300 hPa. Red lines correspond to warm-core composites, blue to cold-core ones. Opaque lines correspond to DJF composites, transparent to JJA ones.

https://doi.org/10.5194/egusphere-2025-6174
Preprint. Discussion started: 17 December 2025

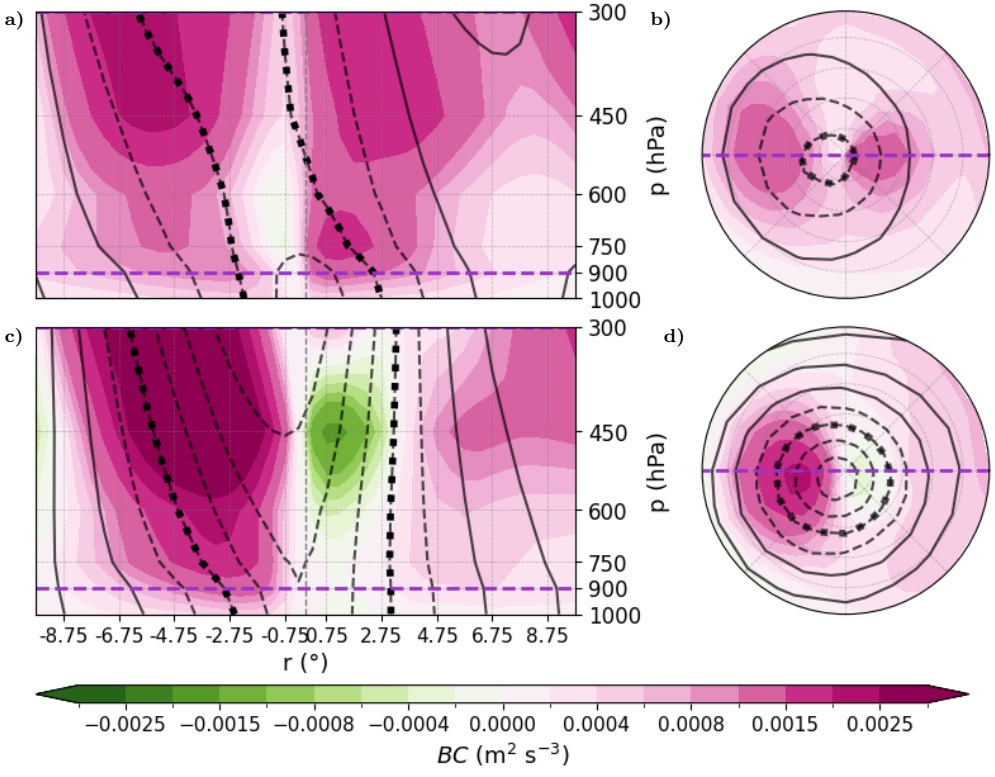

Figure 11. Radial **(b,d)** and vertical **(a,c)** composites of different subsets at SLP min −12 h. Vertical composites are made on the cross section represented by the dashed purple line in panels (b,d). Radial snapshots are means between pressure levels 900 and 300 hPa, represented by dashed purples lines in panels (a,c). **(a,b)** JJA warm cores. **(c,d)** JJA cold cores. In all panels, shading represents BC. Levels are non-linear, the boundaries are: [−30, −25, −20, −15, −10, −8, −6, −4, −2, 0, 2, 4, 8, 10, 15, 20, 25, 30].10^{-3} m^2 s^{-3}. Black contours represent the geopotential anomaly contours, the −40 m value being highlighted by a dotted black line. See Appendix A for more details on the computation of geopotential height anomaly.